Searches for Gravitational Waves from Known Pulsars at Two Harmonics in 2015–2017 LIGO Data

The LIGO Scientific Collaboration, the Virgo Collaboration and Additional authors

(Dated: February 25, 2019)

ABSTRACT

We present a search for gravitational waves from 222 pulsars with rotation frequencies $\gtrsim 10\,\mathrm{Hz}$. We use advanced LIGO data from its first and second observing runs spanning 2015–2017, which provides the highest sensitivity gravitational-wave data so far obtained. In this search we target emission from both the $l = m = 2$ mass quadrupole mode, with a frequency at twice that of the pulsar's rotation, and from the $l = 2$, $m = 1$ mode, with a frequency at the pulsar rotation frequency. The search finds no evidence for gravitational-wave emission from any pulsar at either frequency. For the $l = m = 2$ mode search, we provide updated upper limits on the gravitational-wave amplitude, mass quadrupole moment, and fiducial ellipticity for 167 pulsars, and the first such limits for a further 55. For 20 young pulsars these results give limits that surpass those inferred from the pulsars' spin-down. For the Crab and Vela pulsars our results constrain gravitational-wave emission to account for less than 0.017% and 0.18% of the spin-down luminosity, respectively. For the recycled millisecond pulsar J0711−6830 our limits are only a factor of 1.3 above the spin-down limit, assuming the canonical value of $10^{38}\,\mathrm{kg\,m^2}$ for the star's moment of inertia, and imply a gravitational-wave derived upper limit on the star's ellipticity of 1.2×10^{-8}. We also place new limits on the emission amplitude at the rotation frequency of the pulsars.

Keywords: pulsars: general — stars: neutron — gravitational waves

1. INTRODUCTION

There have been several previous searches for persistent (or continuous) quasi-monochromatic gravitational waves emitted by a selection of known pulsars using data from the LIGO, Virgo, and GEO600 gravitational-wave detectors (Abbott et al. 2004, 2005, 2007, 2008, 2010; Abadie et al. 2011; Aasi et al. 2014; Abbott et al. 2017a). In the majority of these, the signals that have been searched for are those that would be expected from stars with a non-zero $l = m = 2$ mass quadrupole moment Q_{22} and with polarization content consistent with the expectations of General Relativity (see, e.g., Zimmermann & Szedenits 1979; Bonazzola & Gourgoulhon 1996; Jaranowski et al. 1998). Such signals would be produced at twice the stellar rotation frequencies, and searches have generally assumed that the rotation frequency derived from electromagnetic observations of the pulsars is phase locked to the star's rotation and thus the gravitational-wave signal. Some searches have been performed where the assumption of the phase locking to the observed electromagnetic signal has been slightly relaxed, allowing the signal to be potentially offset over a small range of frequencies ($\sim 10-100\,\mathrm{mHz}$) and first fre-

quency derivatives (Abbott et al. 2008; Aasi et al. 2015a; Abbott et al. 2017b). A search including the prospect of the signal's polarization content deviating from the purely tensorial modes predicted by General Relativity has also been performed in Abbott et al. (2018a). None of these searches have detected a gravitational-wave signal from any of the pulsars that were targeted. Thus, stringent upper limits of the gravitational-wave amplitude, mass quadrupole moment, and ellipticity have been set.

Emission of gravitational waves at a pulsar's rotation frequency from the $l = 2$, $m = 1$ harmonic mode, in addition to emission at twice the rotation frequency from the $l = m = 2$ mode, has long been theorized (Zimmermann & Szedenits 1979; Zimmermann 1980; Jones & Andersson 2002). The fiducial emission mechanism would be from a biaxial, or triaxial star, undergoing free precession. In the case of a precessing biaxial star, or a precessing triaxial star with a small "wobble angle", the electromagnetic pulsar emission frequency would be modulated slightly, with the gravitational-wave emission being emitted at frequencies close to once and twice the time-averaged rotation frequency. There is only weak observational evidence for any pulsar showing precession

(see the discussions in, e.g., Jones 2012; Durant et al. 2013, and references therein), and *free* precession would be quickly damped, but as shown in Jones (2010) the existence of a superfluid interior gives rise to the possibility for gravitational-wave emission at the rotation frequency even for a non-precessing star. A search for emission at both once and twice the rotation frequency for 43 pulsars using data from LIGO's fifth science run has been performed in Pitkin et al. (2015). That analysis saw no evidence for signals at the rotation frequency and was consistent with the search conducted for signals purely from the $l = m = 2$ mode (Abbott et al. 2010).

The searches implemented in this work are specifically designed for the case where the signal's phase evolution is very well known over the course of full gravitational-wave detector observing runs. Therefore, here we will only focus on the assumption that emission occurs at precisely once and twice the observed rotation frequency, as given by the model in Jones (2010), so we do not account for the possibility of any of the sources undergoing free precession.

Previous searches, combining the results given in Aasi et al. (2014) and Abbott et al. (2017a), have included a total of 271 pulsars. The most stringent upper limit on gravitational-wave amplitude from the $l = m = 2$ mode was set for PSR J1918−0642 at 1.6×10^{-26}, and the most stringent upper limit on the fiducial ellipticity (see Appendix A, Equations (A2) and (A4)) was

set for PSR J0636+5129 at 1.3×10^{-8} (Abbott et al. 2017a). However, for these particular pulsars, both of which are millisecond pulsars (MSPs), the gravitational-wave amplitude limits are above the fiducial spin-down limit (see Appendix A and Equation (A7)). The observational limits in Abbott et al. (2017a) showed 8 pulsars for which the fiducial spin-down limit was surpassed, with the upper limits on emission from the Crab pulsar (PSR J0534+2200) and Vela pulsar (PSR J0835−4510) being factors of more than 20 and 9 below their respective spin-down limits.

Concurrently with this work, a search has been performed for 33 pulsars using advanced LIGO data from the second observing run in which the assumption of phase locking between the electromagnetically-observed signal and gravitational-wave signal is relaxed by allowing the signal model to vary freely over a narrow band of frequencies and frequency derivatives (Abbott et al., in preparation). Even with the slight sensitivity decrease compared to the analysis presented here, due to the wider parameter space, that analysis surpasses the spin-down limit for 13 of the pulsars.

1.1. *Signal model*

Using the formalism shown in Jones (2015); Pitkin et al. (2015) the gravitational-wave waveform from the $l = 2$, $m = 1$ harmonic mode can be written as

$$h_{21}(t) = -\frac{C_{21}}{2} \left[F_+^D(\alpha, \delta, \psi; t) \sin \iota \cos \iota \cos \left(\Phi(t) + \Phi_{21}^C \right) + F_\times^D(\alpha, \delta, \psi; t) \sin \iota \sin \left(\Phi(t) + \Phi_{21}^C \right) \right], \qquad (1)$$

and that from the $l = m = 2$ mode can be written as

$$h_{22}(t) = -C_{22} \left[F_+^D(\alpha, \delta, \psi; t) \left(1 + \cos^2 \iota \right) \cos \left(2\Phi(t) + \Phi_{22}^C \right) + 2 F_\times^D(\alpha, \delta, \psi; t) \cos \iota \sin \left(2\Phi(t) + \Phi_{22}^C \right) \right]. \qquad (2)$$

Here, C_{21} and C_{22} represent the amplitudes of the components, Φ_{21}^C and Φ_{22}^C represent initial phases at a particular epoch, $\Phi(t)$ is the rotational phase of the source, and ι is the inclination of the source's rotation axis with respect to the line-of-sight.[1] The detected amplitude is modulated by the detector response functions for the two polarizations of the signal ('+' and '×'), $F_+^D(\alpha, \delta, \psi; t)$ and $F_\times^D(\alpha, \delta, \psi; t)$, which depend on the location and orientation of detector D, the location of the source on the sky, defined by the right ascension

α and declination δ, and the polarization angle of the source ψ.

As shown in Jones (2015), the waveforms given in Equations (1) and (2) describe a generic signal, but the amplitudes (C_{21} and C_{22}) and phases (Φ_{21}^C and Φ_{22}^C) can be related to intrinsic physical parameters describing a variety of source models, e.g., a triaxial star spinning about a principal axis (Abbott et al. 2004), a biaxial precessing star (Jones & Andersson 2002), or a triaxial star not spinning about a principal axis (Jones 2010). In the standard case adopted for previous gravitational-wave searches of a triaxial star spinning about a principal axis, there is only emission at twice the rotation frequency from the $l = m = 2$ mode, so only Equation (2) is non-zero. In this case the C_{22} amplitude can be simply

---

[1] For precessing stars the phase evolution $\Phi(t)$ in Equations (1) and (2) will not necessarily be given by the rotational phase, but can differ by the precession frequency.

related to the standard gravitational-wave strain amplitude h_0 via $h_0 = 2C_{22}$.[2] We can simply define the phase Φ_{22}^C as relating to the initial rotational phase ϕ_0 via $\Phi_{22}^C = 2\phi_0$, noting that ϕ_0 actually incorporates the sum of two phase parameters (an initial gravitational-wave phase and another phase offset) that are entirely degenerate and therefore not separately distinguishable (Jones 2015).

Despite Equations (1) and (2) not providing the intrinsic parameters of the source they do break strong degeneracies between them, which are otherwise impossible to disentangle (see Pitkin et al. 2015, showing this for the case of a triaxial source not rotating about a principal axis).

In this work we adopt two analyses. The first assumes the standard picture of a triaxial star rotating around a principal axis from which we can simply relate the waveform amplitude C_{22} to the gravitational-wave amplitude. In this case we can then compare this to the standard spin-down limit, and can calculate each source's mass quadrupole Q_{22} and fiducial ellipticity upper limits (see Appendix A for definitions of these standard quantities.) The second assumes the model of a triaxial star not spinning about a principal axis, for which there could be emission at both once or twice the rotation frequency. In this case we do not attempt to relate the signal amplitudes to any physical parameter of the source.

1.2. Signal strength

For the $l = m = 2$ quadrupole mode the strength of the emission is defined by the size of the mass quadrupole moment Q_{22} (see Equations (A1) and (A3)), which is proportional to the ellipticity of the star, and to the star's moment of inertia, and will therefore depend upon the star's mass, and also upon the equation-of-state of neutron star matter (see, e.g., Ushomirsky et al. 2000; Owen 2005; Johnson-McDaniel & Owen 2013). This ellipticity could be provided by some physical distortion of the star's crust or irregularities in the density profile of the star. For our purposes the mechanism providing the distortion must be sustained over long periods, e.g., the crust must be strong enough for any (sub-millimetre high) mountain to be maintained (see Owen 2005; Johnson-McDaniel & Owen 2013, for discussions of the maximum sustainable ellipticities for various neutron star equations of state), or there must be a persistent strong internal magnetic field (e.g., Bonazzola

& Gourgoulhon 1996; Cutler 2002). Johnson-McDaniel & Owen (2013) suggest that, assuming a standard set of neutron star equations of state, *maximum* fiducial ellipticities of a few 10^{-6} could be sustained. Constraints on the neutron star equation-of-state are now starting to be probed using gravitational-wave observations from the binary neutron star coalescence observed as GW170817 (Abbott et al. 2017c, 2018b). These constraints suggest that softer equations of state are favored over stiffer ones, which would imply smaller maximum crustal quadrupoles. An additional caveat to this is that the maximum crustal deformation is also dependent on the star's mass, and less massive stars would allow larger deformations (Horowitz 2010; Johnson-McDaniel & Owen 2013), so there is still a wide range of uncertainty. Recent work on the strength of neutron star crusts consisting of nuclear pasta suggests that these could have larger breaking strains and thus support larger ellipticities (Caplan et al. 2018).

It has recently been suggested by Woan et al. (2018) that the distribution of MSPs in the period-period derivative plane provides some observational evidence that they may all have a limiting *minimum* ellipticity of $\sim 10^{-9}$. This could be due to some common process that takes place during the recycling accretion stage that spins the pulsar up to millisecond periods. For example, there could be external magnetic field burial (see, e.g., Melatos & Phinney 2001; Payne & Melatos 2004) for which the size of the buried field is roughly the same across all stars, or similar levels of spin-up leading to crust breaking (e.g., Fattoyev et al. 2018). If this is true it provides a compelling reason to look for emission from these objects.

For the model emitting at both $l = 2$, $m = 1, 2$ modes, and assuming no precession, the signal amplitudes are related to combinations of moment of inertia asymmetries and orientation angles between the crust and core of the star (Jones 2010). These are related in a complex way to the C_{21} and C_{22} amplitudes given in Equations (1) and (2) (see Jones 2015). In general, if the Q_{21} and Q_{22} mass moments are equal then the gravitational-wave strain from the $l = 2$, $m = 1$ mode would be roughly four times smaller due to the fact that it is related to the square of the frequency and that mode is at half the frequency of the $l = m = 2$ mode. However, we do not have good estimates of what the actual relative mass moments might be.

1.3. Search methods

As with the previous searches for gravitational waves from known pulsars described in Aasi et al. (2014) and Abbott et al. (2017a), we make use of three semi-

---

[2] To maintain the sign convention between Equation (2) and the equivalent equation in, e.g., Jaranowski et al. (1998), the transform between h_0 and C_{22} should more strictly be $h_0 = -2C_{22}$.

independent search methods. We will not describe these methods in detail here, but refer the reader to Aasi et al. (2014) for more information. Briefly, the three methods are: a search using narrow-banded time-domain data to perform Bayesian parameter estimation for the unknown signal parameters, and marginal likelihood evaluation, for each pulsar (Dupuis & Woan 2005; Pitkin et al. 2017); a search using the same narrow-banded time series, but Fourier-transformed into the frequency domain, to calculate the $\mathcal{F}$-statistic (Jaranowski et al. 1998) (or equivalent $\mathcal{G}$-statistic for constrained orientations Jaranowski & Królak 2010), with a frequentist-based amplitude upper limit estimation procedure (Feldman & Cousins 1998); and, a search in the frequency domain that makes use of splitting of any astrophysical signal into five frequency harmonics through the sidereal amplitude modulation given by the detector responses (Astone et al. 2010, 2012). We call these approaches the *Bayesian*, $\mathcal{F}$-/$\mathcal{G}$-statistic, and 5n-vector methods, respectively. The first of these methods has been applied to all the pulsars in the sample (see Section 2.2), and again following Aasi et al. (2014); Abbott et al. (2017a) at least two of the above methods have been applied to a selection of 34 high-value targets at which the spin-down limit is surpassed or closely approached. The results of the 5n-vector analysis only use data from the LIGO O2 run (see Section 2.1).

All these methods have been adapted to deal with the potential for signals at both once and twice the rotation frequency. For the *Bayesian* method, when searching for such a signal the narrow-banded time series from both frequencies are included in a coherent manner, with common polarization angles ψ and orientations ι. For the 5n-vector and $\mathcal{F}$-/$\mathcal{G}$-statistic methods a simpler approach is taken, and signals at the two frequencies are searched for independently. The $\mathcal{F}$/$\mathcal{G}$-statistic approach for such a signal is described in more detail in Bejger & Królak (2014). As a consequence, given that $C_{21} = 0$ (see Equation (1)) corresponds to the case of a triaxial star rotating around one of its principal axes of inertia, results for the amplitude C_{22} (Equation (2)) from the 5n-vector method are not given as they are equivalent to those for the standard amplitude h_0.

In the case of a pulsar being observed to glitch during the run (see Section 2.2) the methods take different approaches. For the *Bayesian* method it is assumed that any glitch may produce an unknown offset between the electromagnetically observed rotational phase and the gravitational-wave phase. Therefore, an additional phase offset is added to the signal model at the time of the glitch and this is included as a parameter to be estimated, while the gravitational-wave

amplitude and orientation angles of the source (inclination and polarization) are assumed to remain fixed over the glitch. This is consistent with the analysis in Abbott et al. (2010), although differs from the more recent analyses in Aasi et al. (2014); Abbott et al. (2017a) in which each inter-glitch period was treated semi-independently, i.e., independent phases and polarization angles were assumed for each inter-glitch period, but two-dimensional marginalized posterior distributions on the gravitational-wave amplitude and cosine of the inclination angle from data before a glitch was used as a prior on those parameters when analyzing data after the glitch. For both the $\mathcal{F}$/$\mathcal{G}$-statistic and 5n-vector methods, as already done in Aasi et al. (2014); Abbott et al. (2017a), each inter-glitch period is analyzed independently, i.e., no parameters are assumed to be coherent over the glitch, and the resulting statistics are incoherently combined.

The prior probability distributions for the unknown signal parameters, as used for the *Bayesian* and 5n-vector methods, are described in Appendix B.

The 5n-vector method uses a description of the gravitational-wave signal based on the concept of polarization ellipse. The relation of the amplitude parameter H_0 used by the 5n-vector method with both the standard strain amplitude h_0 and the C_{21} amplitude given in Equation (1) is described in Appendix E.

2. DATA

In this section we briefly detail both the gravitational-wave data that has been used in the searches, and the electromagnetic ephemerides for the selection of pulsars that have been included.

2.1. Gravitational-wave data

The data analyzed in this paper consists of that obtained by the two LIGO detectors (the LIGO Hanford Observatory, commonly abbreviated to LHO or H1, and the LIGO Livingston Observatory, abbreviated to LLO or L1) taken during their first (Abbott et al. 2016) and second observing runs (O1 & O2 respectively) in their advanced detector configurations (Aasi et al. 2015b).

Data from O1 between 2015 September 11 (with start times of 01:25:03 UTC and 18:29:03 UTC for LHO and LLO, respectively) and 2016 January 19 at 17:07:59 UTC has been used.[3] The calibration of this data, and the frequency-dependent uncertainties on amplitude and phase over the run, is described in detail in

---

[3] The O1 dataset is publicly available via the Gravitational Wave Open Science Center https://www.gw-openscience.org (Vallisneri et al. 2015).

Cahillane et al. (2017). Over the course of the O1 run the calibration amplitude uncertainty was no larger than 5% and 10%, and the phase uncertainty was no larger than 3° and 4°, for LHO and LLO, respectively, over the frequency range $\sim 10 - 2000$ Hz (these are derived from the 68% confidence levels given in Figure 11 of Cahillane et al. 2017). All data flagged as in "science mode", i.e., when the detectors were operating in a stable state, and for which the calibration was behaving as expected, has been used. This gave a total of 79 d and 66 d observing time for LHO and LLO, respectively, equivalent to duty factors of 60% and 51%.

Data from O2 between 2016 November 30 at 16:00:00 UTC and 2017 August 25 at 22:00:00 UTC, for both LHO and LLO, have been used. An earlier version of the calibrated data for this observing run, and the uncertainty budget associated with it, is again described in Cahillane et al. (2017). However, data with an updated calibration has been produced and used in this analysis, with this having an improved uncertainty budget (Cahillane et al. 2018). Over the course of the O2 run the calibration amplitude uncertainty was no larger than 3% and 8%, and the phase uncertainty was no larger than 3° and 4°, for LHO and LLO, respectively, over the frequency range of $\sim 10 - 2000$ Hz. The data used in this analysis was post-processed to remove spurious jitter noise that affected detector sensitivity across a broad range of frequencies, particularly for data from LHO, and to remove some instrumental spectral lines (Davis et al. 2018; Driggers et al. 2018).

The Virgo gravitational-wave detector (Acernese et al. 2015) was operating during the last 25 days of O2 (Abbott et al. 2017d); however, due to its higher noise levels as compared to the LIGO detectors and the shorter observing time, Virgo data was not included in this analysis.

2.2. *Pulsars*

For this analysis we have gathered ephemerides for 222 pulsars based on radio, X-ray, and γ-ray observations. The observations have used the 42 ft telescope and Lovell telescope at Jodrell Bank (UK), the Mount Pleasant Observatory 26 m telescope (Australia), the Parkes radio telescope (Australia), the Nançay Decimetric Radio Telescope (France), the Molonglo Observatory Synthesis Telescope (Australia), the Arecibo Observatory (Puerto Rico), the Fermi Large Area Telescope (LAT), and the Neutron Star Interior Composition Explorer (NICER). As with the search in Abbott et al. (2017a), the criteria for our selection of pulsars was that they have rotation frequencies greater than 10 Hz, so that they are within the frequency band of greatest sensitivity of the LIGO instruments, and for which the calibration is well characterized. There are in fact three pulsars with rotation frequencies just below 10 Hz that we include (PSRs J0117+5914, J1826−1256, and J2129+1210A), for two of these the spin-down limit was potentially within reach using our data.

The ephemerides have been created using pulse time-of-arrival observations that mainly overlapped with all, or some fraction of, the O1 and O2 observing periods (see Section 2.1), so the timing solutions should provide coherent phase models over and between the two runs. Of the 222, we have 168 for which the electromagnetic timings fully overlapped with the full O1 and O2 runs. There are 12 pulsars for which there is no overlap between electromagnetic observations and the O2 run. These include two pulsars, J1412+7922 (known as Calvera) and J1849−0001, for which we only have X-ray timing observations from after O2 (Bogdanov et al. 2019). For these we have made the reasonable assumption that timing models are coherent for our analysis and that no timing irregularities, such as glitches, are present.

In all previous searches a total of 271 pulsars had been searched for, with 167 of these being timed for this search. For the others sources ephemerides were not available to us for our current analysis. In particular, we do not have up-to-date ephemerides for many of the pulsars in the globular clusters 47 Tucanae and Terzan 5, or the interesting young X-ray pulsar J0537−6910.

2.2.1. *Glitches*

During the course of the O2 period five pulsars exhibited timing glitches. The Vela pulsar (J0835−4510) glitched on 2016 December 12 at 11:36 UTC (Palfreyman 2016; Palfreyman et al. 2018) and the Crab pulsar (J0534+2200) showed a small glitch on 2017 March 27 at around 22:04 UTC (Espinoza et al. 2011).[4] PSR J1028−5819 glitched some time around 2017 May 29, with a best fit glitch time of 01:36 UTC. PSR J1718−3825 experienced a small glitch around 2017 July 2. PSR J0205+6449 experienced four glitches over the period between the start of O1 and end of O2, with glitch epochs of 2015 November 19, 2016 July 1, 2016 October 19, and 2017 May 27. Two of these glitches occurred in the period between O1 and O2, and as such any effect of the glitches on discrepancies between the electromagnetic and gravitational-wave phase would not be independently distinguishable, meaning effectively only three glitches need to be accounted for.

---

[4] http://www.jb.man.ac.uk/pulsar/glitches.html

2.2.2. *Distances and period derivatives*

When calculating results of the searches in terms of the Q_{22} mass quadrupole, fiducial ellipticity, or spin-down limits (see Appendix A) we require the distances to the pulsars. For the majority of pulsars we use "best estimate" distances given in the ATNF Pulsar Catalogue (Manchester et al. 2005).[5] In the majority of cases these are distances based on the observed dispersion measure and calculated using the Galactic electron density distribution model of Yao et al. (2017), although others are based on parallax measurements, or inferred from associations with other objects or flux measurements. The distances used for each pulsar, and the reference for the value used, are given in Tables 1 and 2.

The spin-down limits that we compare our results to (see Appendix A) require a value for the first period derivative $\dot{P}$, or equivalently frequency derivative $\dot{f}$, of the pulsar. The observed spin-down does not necessarily reflect the intrinsic spin-down of the pulsar as it can be contaminated by the relative motion of the pulsar with respect to the observer. This is particularly prevalent for MSPs, which have intrinsically small spin-downs that can be strongly effected, particularly if they are in the core of a globular cluster where significant intra-cluster accelerations can occur, or if they have a large transverse velocity with respect to the Solar System and/or are close (the "Shklovskii effect"; Shklovskii 1970.) The spin-down can also be contaminated by the differential motion of the Solar System and pulsar due to their orbits around the Galaxy. For the non-globular cluster pulsars, if their proper motions and distances are well enough measured, then these effects can be corrected for to give the intrinsic period derivative (see, e.g., Damour & Taylor 1991). For pulsars where the intrinsic period derivative is given in the literature we have used those values (see Tables 1 and 2 for the values and associated references). For further non-globular cluster pulsars for which a transverse velocity and distance is given in the ATNF Pulsar Catalogue, we correct the observed period derivative using the method in Damour & Taylor (1991). In some cases the corrections lead to negative period derivative values, indicating that the true values are actually too small to be confidently constrained. For these cases Table 2 does not give a period derivative value or associated spin-down limit.

As was previously done in Abbott et al. (2017a), for two globular cluster pulsars, J1823−3021A and J1824−2452A, we assume that the observed spin-down

is not significantly contaminated by cluster effects following the discussions in Freire et al. (2011) and Johnson et al. (2013), respectively, so these values are used without any correction. For the other globular cluster pulsars, we again take the approach of Aasi et al. (2014) and Abbott et al. (2017a) and create proxy period derivative values by assuming the stars have characteristic ages of 10^9 years and braking indices of $n = 5$ (i.e., they are braked purely by gravitational radiation from the $l = m = 2$ mode).[6]

2.2.3. *Orientation constraints*

In Ng & Romani (2004) and Ng & Romani (2008) models are fitted to a selection of X-ray observations of pulsar wind nebulae, which are used to provide the orientations of the nebulae. In previous gravitational-wave searches (Abbott et al. 2008, 2010; Aasi et al. 2014; Abbott et al. 2017a) the assumption has been made that the orientation of the wind nebula is consistent with the orientation of its pulsar. In this work we will also follow this assumption and use the fits in (Ng & Romani 2008) as prior constraints on orientation (inclination angle ι and polarization angle ψ) for PSRs J0205+6449, J0534+2200, J0835−4510, J1952+3252, and J2229+6114. This is discussed in more detail in Appendix B. We refer to results based on these constraints as using *restricted* priors.

3. RESULTS

For each pulsar the results presented here are from analyses coherently combining the data from both the LIGO detectors. As described below, we see no strong evidence for a gravitational-wave signal from any pulsar, so we therefore cast our results in terms of upper limits on the gravitational-wave amplitude. These limits are subject to the uncertainties from the detector calibration as described in Section 2.1, as well as statistical uncertainties that are dependent on the particular analysis method used. For the *Bayesian* analysis, statistical uncertainties on the 95% credible upper limits are on the order of 1% (see Figure 12 of Pitkin et al. 2017). For the *5n-vector* method the statistical uncertainty on the upper limits is of the order of 1-5%, depending on the pulsar.

For all pulsars, we present the results of our analyses in terms of several quantities. For the searches includ-

---

[5] Version 1.59 of the catalogue available at http://www.atnf.csiro.au/people/pulsar/psrcat/.

[6] The braking index n defines the power law relation between the pulsar's frequency and frequency derivative via $\dot{f} = -kf^n$, where k is a constant. Purely magnetic dipole braking gives a value of $n = 3$ and purely quadrupole gravitational-wave braking gives $n = 5$. The characteristic age is defined as $\tau = (n-1)^{-1}(f/\dot{f})$.

ing data at both once and twice the rotation frequency and searching for a signal from both the $l = 2$, $m = 1, 2$ modes we present the inferred limits on the C_{21} and C_{22} amplitude parameters given in Equations (1) and (2). For the searches looking only for emission from the $l = m = 2$ mode we present limits on the signal's gravitational-wave strain h_0. For the *Bayesian search* these limits are 95% credible upper bounds derived from the posterior probability distributions. For the *5n-vector* pipeline the upper limits are obtained with an hybrid frequentist/Bayesian approach, described in Appendix D, consisting in evaluating the posterior probability distribution of the signal amplitude H_0, conditioned to the measured value of a detection statistic, and converting it to a 95% credible upper limit on h_0 or C_{21} (see Section 1.3, Appendix E and Aasi et al. (2014) for more details.) Upper limits have been computed assuming both flat and, when information from electromagnetic observation is available, restricted priors on the polarization parameters, as detailed in Section 2.2.3 and Appendix B.

For the purely $l = m = 2$ mode search, we are able to convert these limits into equivalent limits on several derived quantities. In cases where we have an estimate for the pulsar distance (see Section 2.2 and Tables 1 and 2) h_0 can be converted directly into a limit on the Q_{22} mass quadrupole (see Equation (A3)). Under the assumption of a fiducial principal moment of inertia of $I_{zz}^{\text{fid}} = 10^{38}\,\text{kg}\,\text{m}^2$ this can also place a limit on the fiducial ellipticity ε. When we also have a reliable estimate of the intrinsic period derivative, the spin-down limit h_0^{sd} can be calculated (see Equation (A7)) and the ratio of the observed limits on h_0 to this value, $h_0^{95\%}/h_0^{\text{sd}}$, is shown (the square of this value gives the ratio of the limit on the gravitational-wave luminosity to the spin-down luminosity of the pulsar).

For the *Bayesian* method, an odds value giving a ratio of probabilities is also calculated (the base-10 logarithm of which we denote as $\mathcal{O}$, which is equivalent to $\log_{10}\mathcal{O}_{\text{S/I}}$ from Abbott et al. 2017a), where the numerator is the probability of the data being consistent with a coherent signal model in both detectors, and the denominator is the probability of an incoherent signal present in both detectors *or* Gaussian noise in one detector and a signal in the other *or* Gaussian noise being present in both detectors (see Appendix A.3 in Abbott et al. 2017a or Section 2.6 of Pitkin et al. 2017 for more details). These odds can be used to assess when the coherent signal model is favored by the data. The values of $\mathcal{O}$ for each pulsar are shown in Tables 1 and 2, but in all cases the values are negative indicating no pulsars for which the coherent signal model is favored. Also,

examination of the posteriors probability distributions for the amplitude parameters shows that none are significantly disjoint from the probability of the amplitude being zero.

In the *5n-vector* search the significance of each analysis is expressed through a p-value, which is a measure of how compatible the data are with pure noise. It is obtained by empirically computing the noise-only distribution of the detection statistic, over an off-source region, and comparing it to the value of the detection statistic found in the actual analysis. Conventionally, a threshold of 0.01 on the p-value is used to identify potentially interesting candidates: pulsars for which the analysis provides a p-value smaller than the threshold would deserve a deeper study (see also Aasi et al. 2014; Abbott et al. 2017a). The computed p-values are reported in Table 1. For all the analyzed pulsars they are well above the threshold, suggesting that the data are fully compatible with noise.

For the $\mathcal{F}$-/$\mathcal{G}$-*statistic* method false alarm probabilities of obtaining the observed statistic values are calculated. They are derived assuming that for the $\mathcal{F}$-statistic the $2\mathcal{F}$ value has a χ^2 distribution with 4 degrees-of-freedom (Jaranowski et al. 1998) and for the $\mathcal{G}$-statistic the $2\mathcal{G}$ value has a χ^2 distribution with 2 degrees-of-freedom (Jaranowski & Królak 2010). The false alarm probabilities reported in Table 1 are all close to unity and show no strong indication that the statistics deviate from their expected distributions.

The results for the 34 high-value targets are shown in Table 1 and the results for all the other pulsars are shown in Table 2. The 95% credible upper limits on C_{21} and C_{22} for all 222 pulsars from the *Bayesian* analysis are shown as a function of the gravitational-wave emission frequency in Figure 1. Also shown are estimates of the expected sensitivity of the search given representative noise amplitude spectral densities from the O1 and O2 observing runs (see Appendix C for descriptions of how these were produced.) The 95% credible upper limits on h_0 for all 222 pulsars from the search purely for emission from the $l = m = 2$ mode are shown in Figure 2. Figure 2 also shows spin-down limits on the emission as dark triangles, and in the cases where our observed upper limits surpass these the result is highlighted with a circular marker, and is linked to its associated spin-down limit with a vertical line.

Figure 3 shows a histogram of the ratio $h_0^{95\%}/h_0^{\text{sd}}$ from the *Bayesian* analysis for the $l = m = 2$ mode search, for pulsars where it was possible to calculate a spin-down limit. This shows 20 pulsars for which our results surpass the spin-down limit, and 53 for which the results are between one to ten times greater than h_0^{sd}. If we just

look at MSPs then 41 are within a factor of ten of the spin-down limit.[7] The spin-down limits and the Q_{22} and ε values assume a particular distance, intrinsic period derivative, and fiducial moment of inertia of $10^{38}\,\mathrm{kg\,m^2}$, but there can be considerable uncertainties on these values. For example, distances calculated using the Galactic electron density model of Yao et al. (2017) have a 1σ relative error of $\sim 40\%$, with some parts of the sky having several 100% relative errors. The true moment of inertia depends on the pulsar's mass and equation-of-state and could be within a range of roughly $1-3\times10^{38}\,\mathrm{kg\,m^2}$ (see, e.g., Figures 4 and 7 of Worley et al. 2008 and Figures 6 and 7 of Bejger 2013). We do not incorporate these uncertainties into the results we present here, but they should be kept in mind when interpreting the limits.[8] In the case of pulsar distances the references provided in Tables 1 and 2 should be consulted to provide an estimate of the associated uncertainty. These uncertainties dominate the few percent uncertainties arising from the calibration of the gravitational-wave detectors described in Section 2.1.

The $h_0^{95\%}$ results from the *Bayesian* analysis, recast as limits on Q_{22} and the fiducial ellipticity and assuming the distances given in Tables 1 and 2, are shown in Figure 4.

3.1. *Results highlights*

For decades, two of the most intriguing targets in searches for gravitational waves from pulsars have been the Crab and Vela pulsars (J0534+2200 and J0835−4510, respectively), due to their large spin-down luminosities. The spin-down limit on gravitational-wave amplitude for these two pulsars, assuming emission from the $l = m = 2$ mode and with the phase precisely locked to the observed rotational phase, was surpassed using the initial LIGO and Virgo detectors in Abbott et al. (2008) and Abadie et al. (2011), respectively. Using data from the O1 run, the spin-down limit has also been surpassed for these two pulsars in searches where the strict phase locking of the observed rotational phase

and gravitational-wave phase was relaxed (Abbott et al. 2017b).[9]

For the Crab pulsar, this analysis finds an observed 95% limit of $h_0^{95\%} = 1.9\times10^{-26}$ for the *Bayesian* analysis (with consistent values of 2.2×10^{-26} and 2.9×10^{-26} for the $\mathcal{F}$-*statistic* and 5*n-vector* analyses, respectively). This is 0.013 times the spin-down ratio, or, equivalently means that less than 0.017% of the available spin-down luminosity is emitted via gravitational waves (see Equation (A5)). These limits are also well below less naïve spin-down limits that can be calculated by taking into account the power radiated electromagnetically or through particle acceleration (Ostriker & Gunn 1969; Palomba 2000). As shown in Table 1, slightly tighter constraints are possible if one assumes that the orientation of the pulsar matches that derived from the observed orientation of its pulsar wind nebula (see Section 2.2.3). The above h_0 upper limit corresponds to limits on Q_{22} of $7.7\times10^{32}\,\mathrm{kg\,m^2}$ and an equivalent fiducial ellipticity of 1.0×10^{-5}. This mass quadrupole is almost in the range of maximum allowable quadrupoles for standard neutron star equations of state (see discussion in Section 1.2 and Johnson-McDaniel & Owen 2013).

Similarly, for the Vela pulsar, this analysis finds an observed 95% limit of $h_0^{95\%} = 1.4\times10^{-25}$ for the *Bayesian* analysis (with broadly consistent values of 2.6×10^{-25} and 2.3×10^{-25} for the $\mathcal{F}$-*statistic* and 5*n-vector* analyses, respectively). This is 0.042 times the spin-down ratio, or, equivalently, means that less than 0.18% of the available spin-down luminosity is emitted via gravitational waves. The above h_0 upper limit corresponds to limits on Q_{22} of $5.9\times10^{33}\,\mathrm{kg\,m^2}$ and an equivalent fiducial ellipticity of 7.6×10^{-5}.

Of all the pulsars in the analysis the one with the smallest upper limit on h_0 is PSR J1623−2631 (with a rotational frequency of 90.3 Hz and distance of 1.8 kpc), with $h_0^{95\%} = 8.9\times10^{-27}$. The pulsar with the smallest limit on the Q_{22} mass quadrupole is PSR J0636+5129 (with a rotational frequency of 348.6 Hz and distance of 0.21 kpc), with $Q_{22}^{95\%}$ of 4.5×10^{29}, and an equivalent fiducial ellipticity limit of 5.8×10^{-9}. These limits are only a factor of 3.4 above the pulsar's spin-down limit. Of the MSPs in our search (which, as above, we take as any pulsar with $\dot{P} < 10^{-17}$ s/s), the one for which our limit is closest to the spin-down limit is J0711−6830

---

[7] Based on our sample of pulsars with rotation frequencies greater than 10 Hz there is a clear distinction between the MSP and young (or *normal*) population based on a cut in $\dot{P}$ of $10^{-17}\,\mathrm{s\,s^{-1}}$, i.e., we assume any pulsar with a $\dot{P}$ smaller than this is an MSP.

[8] From Equations (A2), (A3), and (A7) it can be seen that fractional uncertainties on distance will scale directly into the uncertainties on ε, Q_{22} and h_0^{sd}. Increasing the value of I_{zz}^{fid} will proportionally decrease the inferred ε value, and increase the inferred spin-down limit by a factor given by the square root of the fractional increase compared to the canonical moment of inertia.

[9] The spin-down limit was surpassed for the Crab pulsar for a similar narrow-band search in Abbott et al. (2008), under the assumption that the orientation was restricted to that derived from the pulsar wind nebula (see Section 2.2.3) and, more recently, in (Aasi et al. 2015a).
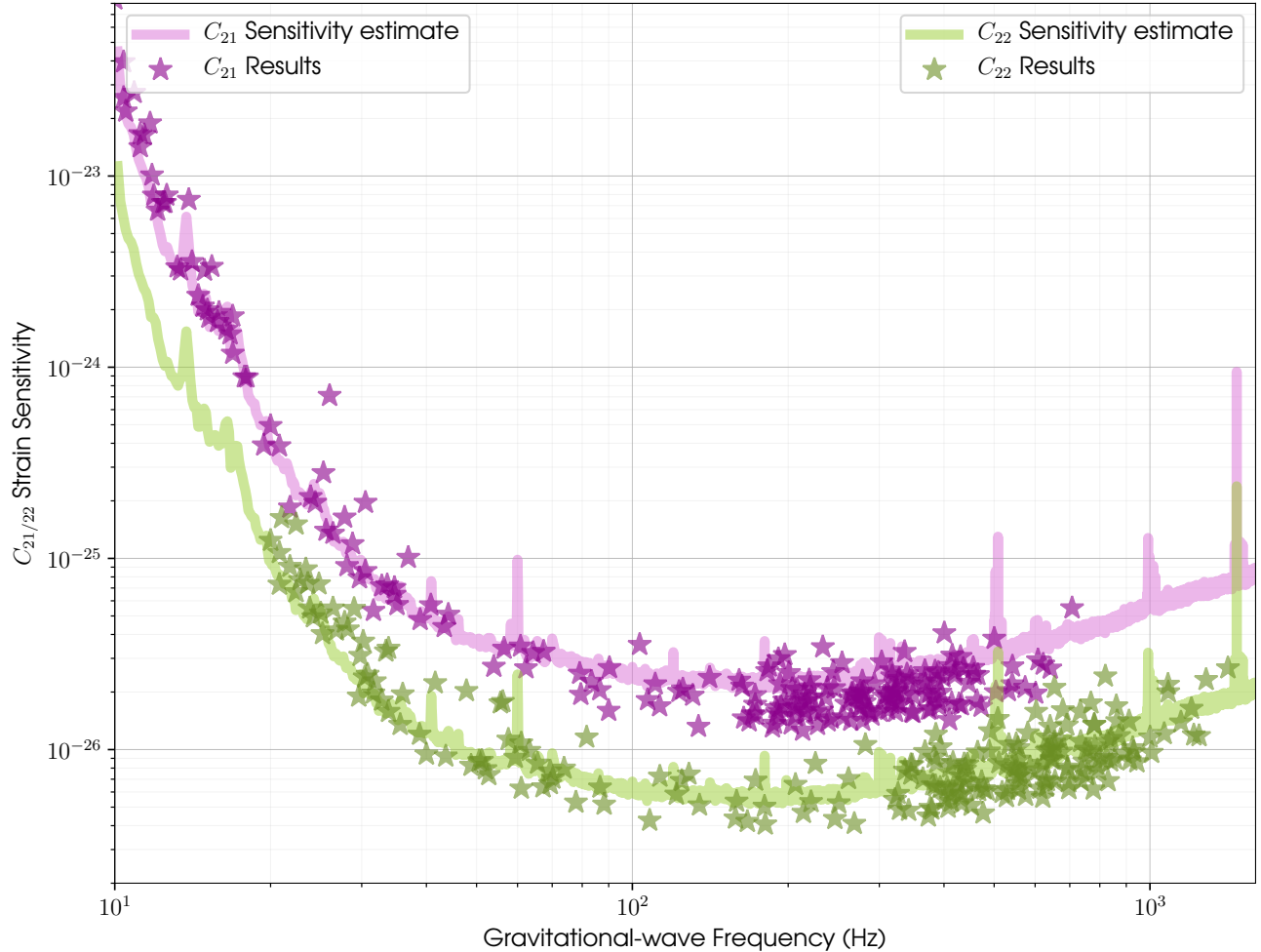
**Figure 1.** Upper limits on C_{21} and C_{22} for 222 pulsars. The stars show the observed 95% credible upper limits on observed amplitudes for each pulsar. The solid lines show an estimate of the expected sensitivity of the searches.

(with a rotational frequency of $182.1\,\mathrm{Hz}$ and distance of $0.11\,\mathrm{kpc}$). It is within a factor of 1.3 of the spin-down limit, with an observed upper limit of $h_0^{95\%} = 1.5\times10^{-26}$ and derived limits on Q_{22} and ellipticity of $9.3\times10^{29}\,\mathrm{kg\,m^2}$ and 1.2×10^{-8}, respectively.[10] The upper bound on possible neutron star moments of inertia is roughly $3\times10^{38}\,\mathrm{kg\,m^2}$, for which the fiducial spin-down limit could be increased a factor of $\sqrt{3} \approx 1.7$, which would be surpassed by our upper limit.

Similarly to Abbott et al. (2017a), our most stringent limits on ellipticity for MSPs still imply limits on the internal toroidal magnetic field strength of $\lesssim 10^9\,\mathrm{T}$ (or $10^{13}\,\mathrm{G}$) (applying Equation (2.4) of Cutler 2002, and assuming a superconducting core). The method in Mastrano & Melatos (2012) could also be applied to these results to constrain the ratio of the poloidal magnetic field energy to the total field energy.

For the searches that include the $l = 2$, $m = 1$ mode, the smallest upper limit on the C_{21} amplitude is for PSR J1744−7619 (with a rotational frequency of $213.3\,\mathrm{Hz}$), at $C_{21}^{95\%} = 1.3\times10^{-26}$. As C_{21} and C_{22} are not very strongly correlated the upper limits on C_{22} are generally consistent with $C_{22}^{95\%} \approx h_0^{95\%}/2$.

---

[10] It is interesting to note that in Abbott et al. (2017a) PSR J0437−4715 was the MSP with an observed upper limit closest to its spin-down limit, being only a factor of 1.4 above that value, while J0711−6830 had a limit that was a factor of ~ 20 above its spin-down limit. For J0437−4715, despite now having an improved upper limit on the gravitational-wave amplitude, the correction of the observed period derivative to the intrinsic period derivative has lowered the spin-down limit by roughly a factor of two. For J0711−6830 the distance estimated using the YMW16 Galactic electron density model (Yao et al. 2017) is about a factor of 9 closer than that estimated with the previously used NE2001 model (Cordes & Lazio 2002).
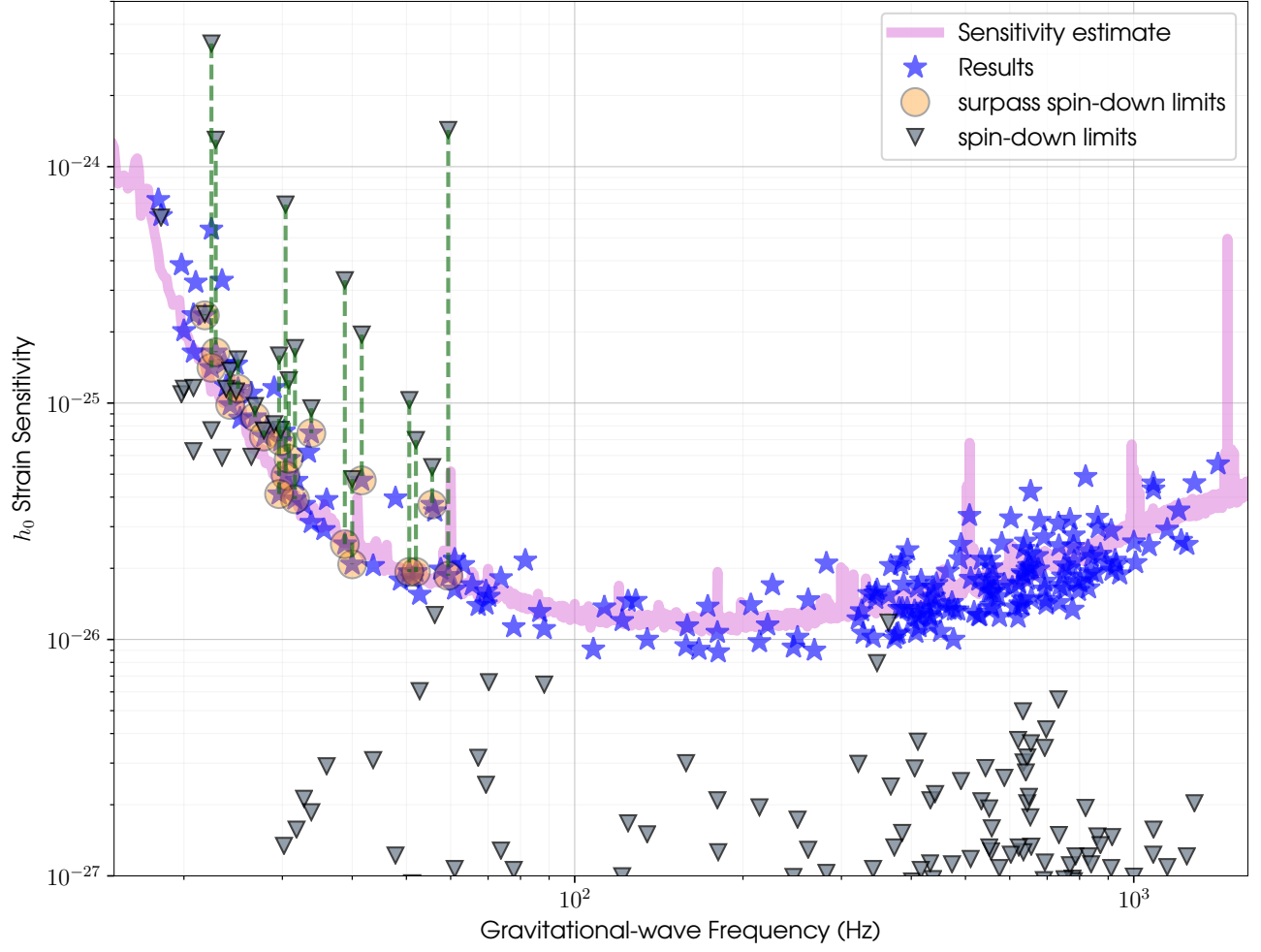
Figure 2. Upper limits on h_0 for 222 pulsars. The stars show the observed 95% credible upper limits on observed amplitude for each pulsar. The solid line shows an estimate of the expected sensitivity of the search. Triangles show the limits on gravitational-wave amplitude derived from each pulsar's observed spin-down.
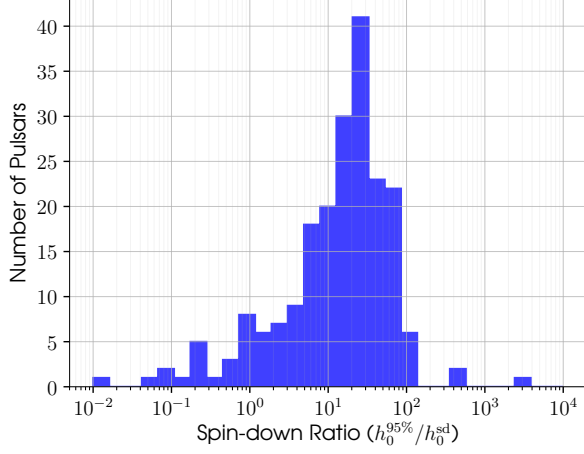
Figure 3. Histogram of ratios of upper limits on h_0 compared to the spin-down limit.
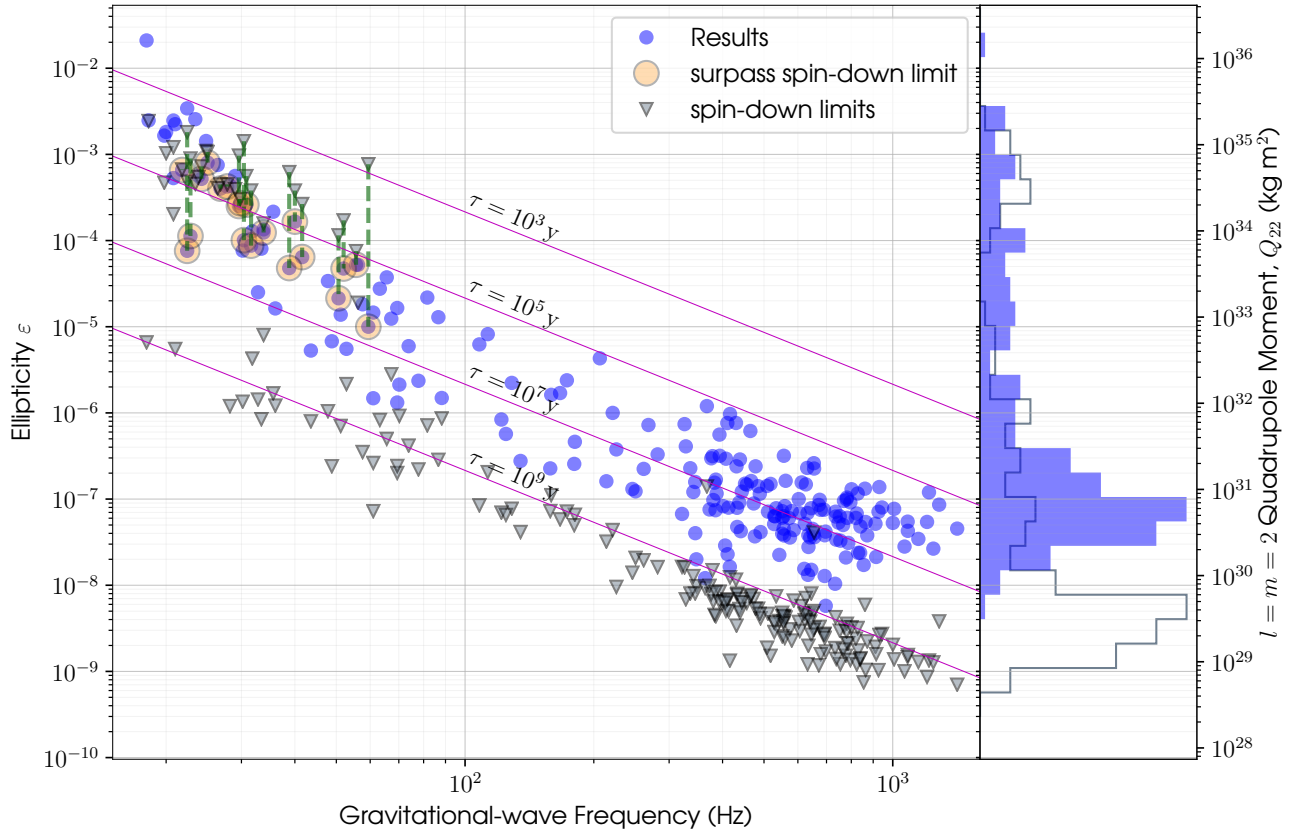
Figure 4. Upper limits on mass quadrupole Q_{22} and fiducial ellipticity ε for 222 pulsars. The filled circles show the limits as derived from the observed upper limits on the gravitational-wave amplitude h_0 assuming the canonical moment of inertia and distances given in Tables 1 and 2. Triangles show the limits based derived from each pulsar's observed spin-down. The diagonal lines show contours of equal characteristic age τ assuming braking is entire through gravitational-wave emission.

Table 1. Limits on Gravitational-wave Amplitude, and Other Derived Quantities, for 34 High-value Pulsars from the Three Analysis Methods.

Pulsar Name (J2000)	$f_{\rm rot}$ (Hz)	$\dot{P}_{\rm rot}$ (s s^{-1})	Distance (kpc)	$h_0^{\rm sd}$	Analysis Method	$C_{21}^{95\%}$	$C_{22}^{95\%}$	$h_0^{95\%}$	$Q_{22}^{95\%}$ (kg m^2)	$\varepsilon^{95\%}$	$h_0^{95\%}/h_0^{\rm sd}$	Statistic[2] $l{=}2,m{=}1,2$	Statistic[2] $l{=}2,m{=}2$	Statistic[3] $l{=}2,m{=}2$
J0030+0451	205.5	1.1×10^{-20}[g]	0.33[a]	3.7×10^{-27}	Bayesian	1.7×10^{-26}	5.9×10^{-27}	1.3×10^{-26}	1.8×10^{30}	2.3×10^{-8}	3.4	-3.8	-2.1	$\cdots$
					$\mathcal{F}$-statistic	$\cdots$	$\cdots$	$\cdots$	$\cdots$	$\cdots$	$\cdots$	$\cdots$	$\cdots$	$\cdots$
					$5n$-vector	1.3×10^{-26}	$\cdots$	1.7×10^{-26}	2.3×10^{30}	3.0×10^{-8}	4.5	0.72	$\cdots$	0.61
J0117+5914[1]	9.9	5.9×10^{-15}	1.77[b]	1.1×10^{-25}	Bayesian	$\cdots$	$\cdots$	3.8×10^{-25}	1.3×10^{35}	1.7×10^{-3}	3.5	-2.4	-1.9	$\cdots$
					$\mathcal{F}$-statistic	$\cdots$	$\cdots$	$\cdots$	$\cdots$	$\cdots$	$\cdots$	$\cdots$	$\cdots$	$\cdots$
					$5n$-vector	$\cdots$	$\cdots$	2.6×10^{-25}	8.6×10^{34}	1.1×10^{-3}	2.4	$\cdots$	$\cdots$	0.31
J0205+6449[1]	15.2	1.9×10^{-13}	2.00[c]	6.9×10^{-25}	Bayesian	$1.8(1.5)\times10^{-24}$	$2.4(3.6)\times10^{-26}$	$4.9(7.1)\times10^{-26}$	$0.8(1.1)\times10^{33}$	$1.0(1.5)\times10^{-4}$	0.071(0.1)	$-4.8(-4.6)$	$-2.7(-2.4)$	$\cdots$
					$\mathcal{F}$-statistic	2.2×10^{-24}	4.5×10^{-26}	8.8×10^{-26}	1.4×10^{34}	1.8×10^{-4}	0.13	0.71	0.26	$\cdots$
					$5n$-vector	$\cdots$	$\cdots$	$2.9(4.5)\times10^{-26}$	$4.6(7.1)\times10^{33}$	$5.9(9.2)\times10^{-5}$	0.042(0.065)	$\cdots$	$\cdots$	0.41
J0534+2200[1]	29.7	4.2×10^{-13}	2.00	1.4×10^{-24}	Bayesian	$7.9(5.8)\times10^{-26}$	$9.1(7.3)\times10^{-27}$	$1.9(1.5)\times10^{-26}$	$7.7(6.0)\times10^{32}$	$1.0(0.8)\times10^{-5}$	0.013(0.01)	$-5.1(-5.2)$	$-2.6(-2.7)$	$\cdots$
					$\mathcal{F}$-statistic	$1.6(1.1)\times10^{-25}$	$1.1(1.1)\times10^{-26}$	$2.2(1.3)\times10^{-26}$	$9.1(5.4)\times10^{32}$	$1.2(0.7)\times10^{-5}$	0.015(0.0091)	0.32(0.18)	0.65(0.87)	$\cdots$
					$5n$-vector	$1.7(1.3)\times10^{-25}$	$\cdots$	$2.9(2.9)\times10^{-26}$	$1.2(1.2)\times10^{33}$	$1.6(1.6)\times10^{-5}$	0.02(0.02)	0.70	$\cdots$	0.45
J0711$-$6830[1]	182.1	1.4×10^{-20}	0.11[b]	1.2×10^{-26}	Bayesian	2.6×10^{-26}	7.0×10^{-27}	1.5×10^{-26}	9.3×10^{29}	1.2×10^{-8}	1.3	-3.1	-1.9	$\cdots$
					$\mathcal{F}$-statistic	$\cdots$	$\cdots$	$\cdots$	$\cdots$	$\cdots$	$\cdots$	$\cdots$	$\cdots$	$\cdots$
					$5n$-vector	1.2×10^{-26}	$\cdots$	1.5×10^{-26}	9.1×10^{29}	1.2×10^{-8}	1.3	0.79	$\cdots$	0.39
J0835$-$4510[1]	11.2	1.2×10^{-13}	0.29[j]	3.3×10^{-24}	Bayesian	$1.4(1.1)\times10^{-23}$	$6.7(6.2)\times10^{-26}$	$1.4(1.2)\times10^{-25}$	$5.9(5.2)\times10^{33}$	$7.6(6.7)\times10^{-5}$	0.042(0.037)	$-4.2(-4.4)$	$-2.5(-2.8)$	$\cdots$
					$\mathcal{F}$-statistic	$1.3(1.1)\times10^{-23}$	$1.1(0.9)\times10^{-25}$	$2.6(2.0)\times10^{-25}$	$1.1(0.8)\times10^{34}$	$1.4(1.1)\times10^{-4}$	0.078(0.06)	0.75(0.75)	0.75(0.75)	$\cdots$
					$5n$-vector	$\cdots$	$\cdots$	$2.3(2.4)\times10^{-25}$	$9.7(9.9)\times10^{33}$	$1.3(1.3)\times10^{-4}$	0.07(0.071)	$\cdots$	$\cdots$	0.41
J0940$-$5428	11.4	3.3×10^{-14}	0.38[b]	1.3×10^{-24}	Bayesian	1.6×10^{-23}	7.7×10^{-26}	1.6×10^{-25}	8.7×10^{33}	1.1×10^{-4}	0.13	-3.7	-2.3	$\cdots$
					$\mathcal{F}$-statistic	$\cdots$	$\cdots$	$\cdots$	$\cdots$	$\cdots$	$\cdots$	$\cdots$	$\cdots$	$\cdots$
					$5n$-vector	$\cdots$	$\cdots$	1.7×10^{-25}	8.9×10^{33}	1.2×10^{-4}	0.13	$\cdots$	$\cdots$	0.70
J1028$-$5819	10.9	1.6×10^{-14}	1.42[b]	2.4×10^{-25}	Bayesian	2.7×10^{-23}	9.1×10^{-26}	2.3×10^{-25}	5.1×10^{34}	6.6×10^{-4}	0.98	-3.5	-2.2	$\cdots$
					$\mathcal{F}$-statistic	$\cdots$	$\cdots$	$\cdots$	$\cdots$	$\cdots$	$\cdots$	$\cdots$	$\cdots$	$\cdots$
					$5n$-vector	$\cdots$	$\cdots$	1.9×10^{-25}	4.1×10^{34}	5.3×10^{-4}	0.8	$\cdots$	$\cdots$	0.40
J1105$-$6107	15.8	1.6×10^{-14}	2.36[b]	1.7×10^{-25}	Bayesian	1.7×10^{-24}	2.0×10^{-26}	3.9×10^{-26}	6.7×10^{33}	8.7×10^{-5}	0.23	-4.6	-2.8	$\cdots$
					$\mathcal{F}$-statistic	$\cdots$	$\cdots$	$\cdots$	$\cdots$	$\cdots$	$\cdots$	$\cdots$	$\cdots$	$\cdots$
					$5n$-vector	$\cdots$	$\cdots$	2.7×10^{-26}	4.6×10^{33}	6.0×10^{-5}	0.16	$\cdots$	$\cdots$	0.93
J1112$-$6103	15.4	3.1×10^{-14}	4.50[b]	1.2×10^{-25}	Bayesian	3.4×10^{-24}	2.5×10^{-26}	5.8×10^{-26}	2.0×10^{34}	2.6×10^{-4}	0.47	-4.2	-3.4	$\cdots$
					$\mathcal{F}$-statistic	$\cdots$	$\cdots$	$\cdots$	$\cdots$	$\cdots$	$\cdots$	$\cdots$	$\cdots$	$\cdots$
					$5n$-vector	$\cdots$	$\cdots$	3.6×10^{-26}	1.2×10^{34}	1.6×10^{-4}	0.29	$\cdots$	$\cdots$	0.76

Table 1 continued

Table 1 (*continued*)

Pulsar Name (J2000)	$f_{\rm rot}$ (Hz)	$\dot{P}_{\rm rot}$ (s s^{-1})	Distance (kpc)	$h_0^{\rm sd}$	Analysis Method	$C_{21}^{95\%}$	$C_{22}^{95\%}$	$h_0^{95\%}$	$Q_{22}^{95\%}$ (kg m^2)	$\varepsilon^{95\%}$	$h_0^{95\%}/h_0^{\rm sd}$	Statistic^2 $l=2,m=1,2$	Statistic^3 $l=2,m=2$
J1410−6132	20.0	3.2×10^{-14}	$13.51^{\rm b}$	4.8×10^{-26}	Bayesian	4.9×10^{-25}	9.4×10^{-27}	2.1×10^{-26}	1.3×10^{34}	1.7×10^{-4}	0.44	-5.7	-3.0
					$\mathcal{F}$-statistic	…	…	…	…	…	…	…	…
					$5n$-vector	5.4×10^{-25}	…	2.6×10^{-26}	1.6×10^{34}	2.1×10^{-4}	0.55	…	0.88
J1412+7922	16.9	3.3×10^{-15}	$2.00^{\rm o}$	9.5×10^{-26}	Bayesian	1.8×10^{-24}	3.4×10^{-26}	7.5×10^{-26}	9.6×10^{33}	1.2×10^{-4}	0.78	-4.9	-2.1
					$\mathcal{F}$-statistic	2.3×10^{-24}	2.2×10^{-26}	6.2×10^{-26}	7.9×10^{33}	1.0×10^{-4}	0.65	0.24	0.39
					$5n$-vector	…	…	3.6×10^{-26}	4.6×10^{33}	6.0×10^{-5}	0.38	…	0.80
J1420−6048	14.8	8.3×10^{-14}	$5.63^{\rm b}$	1.6×10^{-25}	Bayesian	2.1×10^{-24}	1.9×10^{-26}	4.1×10^{-26}	1.9×10^{34}	2.5×10^{-4}	0.26	-6.2	-2.8
					$\mathcal{F}$-statistic	…	…	…	…	…	…	…	…
					$5n$-vector	…	…	7.6×10^{-26}	3.6×10^{34}	4.7×10^{-4}	0.48	…	0.52
J1509−5850	11.2	9.2×10^{-15}	$3.37^{\rm b}$	7.7×10^{-26}	Bayesian	1.7×10^{-23}	1.5×10^{-25}	5.4×10^{-25}	2.6×10^{35}	3.4×10^{-3}	7.1	-3.5	-2.0
					$\mathcal{F}$-statistic	…	…	…	…	…	…	…	…
					$5n$-vector	…	…	2.1×10^{-25}	1.0×10^{35}	1.3×10^{-3}	2.7	…	0.72
J1531−5610	11.9	1.4×10^{-14}	$2.84^{\rm b}$	1.1×10^{-25}	Bayesian	7.9×10^{-24}	5.5×10^{-26}	1.2×10^{-25}	4.4×10^{34}	5.6×10^{-4}	1	-4.2	-2.4
					$\mathcal{F}$-statistic	…	…	…	…	…	…	…	…
					$5n$-vector	…	…	1.4×10^{-25}	5.3×10^{34}	6.8×10^{-4}	1.2	…	0.31
J1718−3825	13.4	1.3×10^{-14}	$3.49^{\rm b}$	9.7×10^{-26}	Bayesian	3.2×10^{-24}	4.2×10^{-26}	8.7×10^{-26}	3.1×10^{34}	4.0×10^{-4}	0.9	-5.6	-2.4
					$\mathcal{F}$-statistic	…	…	…	…	…	…	…	…
					$5n$-vector	…	…	6.5×10^{-26}	2.3×10^{34}	3.0×10^{-4}	0.67	…	0.67
J1809−1917	12.1	2.6×10^{-14}	$3.27^{\rm b}$	1.4×10^{-25}	Bayesian	6.6×10^{-24}	4.9×10^{-26}	9.8×10^{-26}	4.0×10^{34}	5.2×10^{-4}	0.72	-4.4	-2.5
					$\mathcal{F}$-statistic	6.2×10^{-24}	6.2×10^{-26}	7.3×10^{-26}	3.0×10^{34}	3.9×10^{-4}	0.53	0.76	0.76
					$5n$-vector	…	…	1.1×10^{-25}	4.3×10^{34}	5.6×10^{-4}	0.77	…	0.19
J1813−1246	20.8	1.8×10^{-14}	$2.50^{\rm z}$	1.9×10^{-25}	Bayesian	3.9×10^{-25}	2.2×10^{-26}	4.7×10^{-26}	5.0×10^{33}	6.4×10^{-5}	0.24	-4.2	-2.2
					$\mathcal{F}$-statistic	3.8×10^{-25}	1.0×10^{-26}	3.3×10^{-26}	3.5×10^{33}	4.5×10^{-5}	0.17	0.08	0.73
					$5n$-vector	1.0×10^{-24}	…	4.5×10^{-26}	4.7×10^{33}	6.1×10^{-5}	0.23	…	0.22
J1826−1256	9.1	1.2×10^{-13}	$1.39^{\rm cc}$	6.1×10^{-25}	Bayesian	…	…	6.2×10^{-25}	1.9×10^{35}	2.5×10^{-3}	1	-2.0	-2.1
					$\mathcal{F}$-statistic	…	…	…	…	…	…	…	…
					$5n$-vector	…	…	4.7×10^{-25}	1.5×10^{35}	1.9×10^{-3}	0.77	…	…
J1828−1101	13.9	1.5×10^{-14}	$4.77^{\rm b}$	7.7×10^{-26}	Bayesian	7.5×10^{-24}	4.6×10^{-26}	7.2×10^{-26}	3.3×10^{34}	4.2×10^{-4}	0.94	-4.6	-2.5
					$\mathcal{F}$-statistic	…	…	…	…	…	…	…	…
					$5n$-vector	…	…	5.5×10^{-26}	2.5×10^{34}	3.2×10^{-4}	0.71	…	0.13

Table 1 continued

13

Table 1 (*continued*)

Pulsar Name (J2000)	$f_{\rm rot}$ (Hz)	$\dot{P}_{\rm rot}$ (s s^{-1})	Distance (kpc)	$h_0^{\rm sd}$	Analysis Method	$C_{21}^{95\%}$	$C_{22}^{95\%}$	$h_0^{95\%}$	$Q_{22}^{95\%}$ (kg m^2)	$\varepsilon^{95\%}$	$h_0^{95\%}/h_0^{\rm sd}$	Statistic[2] $l{=}2,m{=}1,2$	Statistic[3] $l{=}2,m{=}2$
J1831−0952	14.9	8.3×10^{-15}	$3.68^{\rm b}$	7.7×10^{-26}	Bayesian	3.2×10^{-24}	3.1×10^{-26}	6.9×10^{-26}	2.1×10^{34}	2.7×10^{-4}	0.9	−5.0	−2.4
					$\mathcal{F}$-statistic	...	...	...	...	...	...	...	...
					$5n$-vector	...	...	4.3×10^{-26}	1.3×10^{34}	1.7×10^{-4}	0.56	...	0.75
J1833−0827[1]	11.7	9.2×10^{-15}	$4.50^{\rm m}$	5.9×10^{-26}	Bayesian	1.9×10^{-23}	8.8×10^{-26}	3.3×10^{-25}	2.0×10^{35}	2.6×10^{-3}	5.6	−3.3	−1.9
					$\mathcal{F}$-statistic	...	...	...	...	...	...	...	...
					$5n$-vector	...	...	1.4×10^{-25}	8.3×10^{34}	1.1×10^{-3}	2.3	...	0.94
J1837−0604	10.4	4.5×10^{-14}	$4.77^{\rm b}$	1.2×10^{-25}	Bayesian	4.0×10^{-23}	1.1×10^{-25}	2.4×10^{-25}	1.9×10^{35}	2.5×10^{-3}	2	−3.7	−2.3
					$\mathcal{F}$-statistic	...	...	...	...	...	...	...	...
					$5n$-vector	...	...	1.6×10^{-25}	1.3×10^{35}	1.6×10^{-3}	1.4	...	0.38
J1849−0001	26.0	1.4×10^{-14}	$7.00^{\rm dd}$	7.0×10^{-26}	Bayesian	7.1×10^{-25}	7.9×10^{-27}	1.9×10^{-26}	3.7×10^{33}	4.7×10^{-5}	0.28	−3.4	−2.6
					$\mathcal{F}$-statistic	6.8×10^{-25}	9.1×10^{-27}	2.8×10^{-26}	5.3×10^{33}	6.9×10^{-5}	0.4	0.04	0.75
					$5n$-vector	6.8×10^{-26}	...	2.0×10^{-26}	3.8×10^{33}	4.9×10^{-5}	0.29	0.23	0.49
J1856+0245	12.4	6.2×10^{-14}	$6.32^{\rm b}$	1.1×10^{-25}	Bayesian	7.2×10^{-24}	7.3×10^{-26}	1.5×10^{-25}	1.1×10^{35}	1.4×10^{-3}	1.3	−3.8	−2.1
					$\mathcal{F}$-statistic	...	...	...	...	...	...	...	...
					$5n$-vector	...	...	1.6×10^{-25}	1.2×10^{35}	1.6×10^{-3}	1.5	...	0.36
J1913+1011	27.8	3.4×10^{-15}	$4.61^{\rm b}$	5.4×10^{-26}	Bayesian	1.6×10^{-25}	1.8×10^{-26}	3.7×10^{-26}	4.0×10^{33}	5.2×10^{-5}	0.7	−4.1	−2.2
					$\mathcal{F}$-statistic	...	...	...	...	...	...	...	...
					$5n$-vector	1.7×10^{-25}	...	2.1×10^{-26}	2.3×10^{33}	3.0×10^{-5}	0.39	0.56	0.90
J1925+1720	13.2	1.0×10^{-14}	$5.06^{\rm b}$	5.9×10^{-26}	Bayesian	3.3×10^{-24}	5.5×10^{-26}	1.1×10^{-25}	5.8×10^{34}	7.5×10^{-4}	1.9	−5.6	−2.4
					$\mathcal{F}$-statistic	...	...	...	...	...	...	...	...
					$5n$-vector	...	...	1.1×10^{-25}	5.8×10^{34}	7.5×10^{-4}	1.9	...	0.44
J1928+1746	14.5	1.3×10^{-14}	$4.34^{\rm b}$	8.1×10^{-26}	Bayesian	2.4×10^{-24}	5.5×10^{-26}	1.2×10^{-25}	4.3×10^{34}	5.6×10^{-4}	1.4	−5.2	−2.6
					$\mathcal{F}$-statistic	2.2×10^{-24}	3.9×10^{-26}	1.3×10^{-25}	4.9×10^{34}	6.3×10^{-4}	1.6	0.61	0.61
					$5n$-vector	...	...	8.6×10^{-26}	3.2×10^{34}	4.2×10^{-4}	1.1	...	0.59
J1935+2025	12.5	6.1×10^{-14}	$4.60^{\rm b}$	1.5×10^{-25}	Bayesian	7.3×10^{-24}	5.2×10^{-26}	1.1×10^{-25}	6.2×10^{34}	8.0×10^{-4}	0.75	−4.4	−2.4
					$\mathcal{F}$-statistic	5.0×10^{-24}	5.5×10^{-26}	1.3×10^{-25}	7.0×10^{34}	9.1×10^{-4}	0.85	0.71	0.71
					$5n$-vector	...	...	1.4×10^{-25}	7.6×10^{34}	9.8×10^{-4}	0.92	...	0.37
J1952+3252[1]	25.3	5.8×10^{-15}	$3.00^{\rm m}$	1.0×10^{-25}	Bayesian	$2.8(2.9)\times10^{-25}$	$8.7(9.0)\times10^{-27}$	$1.9(1.8)\times10^{-26}$	$1.7(1.5)\times10^{33}$	$2.1(2.0)\times10^{-5}$	0.19(0.17)	−3.4(−3.5)	−2.7(−2.6)
					$\mathcal{F}$-statistic	...	...	...	...	...	...	...	...
					$5n$-vector	$2.0(2.0)\times10^{-25}$	...	$2.4(2.5)\times10^{-26}$	$2.1(2.1)\times10^{33}$	$2.7(2.7)\times10^{-5}$	0.24(0.24)	0.06	0.70

Table 1 continued

Table 1 *(continued)*

Pulsar Name (J2000)	$f_{\rm rot}$ (Hz)	$\dot{P}_{\rm rot}$ (s s^{-1})	Distance (kpc)	$h_0^{\rm sd}$	Analysis Method	$C_{21}^{95\%}$	$C_{22}^{95\%}$	$h_0^{95\%}$	$Q_{22}^{95\%}$ (kg m^2)	$\varepsilon^{95\%}$	$h_0^{95\%}/h_0^{\rm sd}$	Statistic^2 $l=2,m=1,2$	Statistic^3 $l=2,m=2$
J2043+2740	10.4	1.3×10^{-15}	$1.48^{\rm b}$	6.3×10^{-26}	Bayesian	2.6×10^{-23}	7.3×10^{-26}	1.6×10^{-25}	4.1×10^{34}	5.3×10^{-4}	2.6	-4.2	-2.5
					$\mathcal{F}$-statistic	2.1×10^{-23}	6.4×10^{-26}	2.8×10^{-25}	7.0×10^{34}	9.1×10^{-4}	4.5	0.79	0.79
					$5n$-vector	$\cdots$	$\cdots$	1.9×10^{-25}	4.7×10^{34}	6.1×10^{-4}	3	$\cdots$	0.17
J2124−3358	202.8	9.0×10^{-21}g	$0.38^{\rm g}$	2.9×10^{-27}	Bayesian	1.4×10^{-26}	6.3×10^{-27}	1.3×10^{-26}	2.2×10^{30}	2.9×10^{-8}	4.6	-3.8	-2.2
					$\mathcal{F}$-statistic	$\cdots$	$\cdots$	$\cdots$	$\cdots$	$\cdots$	$\cdots$	$\cdots$	$\cdots$
					$5n$-vector	2.6×10^{-26}	$\cdots$	1.3×10^{-26}	2.2×10^{30}	2.8×10^{-8}	4.5	0.58	0.58
J2229+6114	19.4	7.8×10^{-14}	$3.00^{\rm hh}$	3.3×10^{-25}	Bayesian	$3.9(3.7)\times10^{-25}$	$1.2(0.8)\times10^{-26}$	$2.5(1.6)\times10^{-26}$	$3.7(2.3)\times10^{33}$	$4.8(3.0)\times10^{-5}$	0.077(0.048)	-5.0(-5.1)	-2.8(-2.9)
					$\mathcal{F}$-statistic	5.6×10^{-25}	2.9×10^{-26}	2.1×10^{-26}	3.1×10^{33}	4.0×10^{-5}	0.063	0.55	0.43
					$5n$-vector	$\cdots$	$\cdots$	$2.5(1.9)\times10^{-26}$	$3.7(2.8)\times10^{33}$	$4.8(3.6)\times10^{-5}$	0.077(0.057)	$\cdots$	0.99
J2302+4442^1	192.6	1.4×10^{-20}	$0.86^{\rm b}$	1.5×10^{-27}	Bayesian	1.5×10^{-26}	6.5×10^{-27}	1.4×10^{-26}	5.7×10^{30}	7.4×10^{-8}	8.9	-3.9	-2.0
					$\mathcal{F}$-statistic	2.5×10^{-26}	5.6×10^{-27}	1.1×10^{-26}	4.7×10^{30}	6.0×10^{-8}	7.2	0.49	0.49
					$5n$-vector	$\cdots$	$\cdots$	$\cdots$	$\cdots$	$\cdots$	$\cdots$	$\cdots$	$\cdots$

NOTE—For references and other notes see Table 2. Values in parentheses are those produced using the restricted orientation priors described in Section 2.2.3.

^{1} The observed $\dot{P}$ has been corrected to account for the relative motion between the pulsar and observer.

^{2} For the *Bayesian* method this column show the base-10 logarithm of the Bayesian odds comparing a coherent signal model at both the $l=2$, $m=1$, 2 modes to incoherent signal models. For the $\mathcal{F}$-/$\mathcal{G}$-statistic method this column shows the false alarm probability for a signal just at the $l=2$, $m=1$ mode, assuming that the $2\mathcal{F}$ value has a χ^2 distribution with 4 degrees-of-freedom and the $2\mathcal{G}$ value has a χ^2 distribution with 2 degrees-of-freedom. For the $5n$-vector method this column show the p-value for a search for a signal at just the $l=2$, $m=1$ mode, where the null hypothesis being tested is that the data is consistent with pure Gaussian noise.

^{3} This is the same a in ^{2}, but for all the methods the assumed signal model is from the $l=m=2$ mode.

Table 2. Limits on Gravitational-wave Amplitude, and Other Derived Quantities, for 188 Pulsars from the *Bayesian* Analysis.

Pulsar Name (J2000)	$f_{\rm rot}$ (Hz)	$\dot{P}_{\rm rot}$ (s s^{-1})	Distance (kpc)	$h_0^{\rm sd}$	$C_{21}^{95\%}$	$C_{22}^{95\%}$	$h_0^{95\%}$	$Q_{22}^{95\%}$ (kg m^2)	$\varepsilon^{95\%}$	$h_0^{95\%}/h_0^{\rm sd}$	$\mathcal{O}_{m=1,2}^{l=2}$	$\mathcal{O}_{m=2}^{l=2}$
J0023+0923[1]	327.8	1.0×10^{-20}	$1.10^{\rm a}$	1.3×10^{-27}	2.4×10^{-26}	6.8×10^{-27}	1.5×10^{-26}	2.8×10^{30}	3.6×10^{-8}	11	-3.9	-2.2
J0034−0534[1]	532.7	4.2×10^{-21}	$1.35^{\rm b}$	8.9×10^{-28}	2.0×10^{-26}	1.2×10^{-26}	2.5×10^{-26}	2.2×10^{30}	2.8×10^{-8}	28	-4.1	-2.1
J0101−6422[1]	388.6	3.8×10^{-21}	$1.00^{\rm b}$	9.7×10^{-28}	2.3×10^{-26}	6.2×10^{-27}	1.3×10^{-26}	1.6×10^{30}	2.1×10^{-8}	14	-4.1	-2.3
J0102+4839	337.4	1.1×10^{-20}	$2.38^{\rm b}$	6.6×10^{-28}	1.9×10^{-26}	9.8×10^{-27}	2.0×10^{-26}	7.6×10^{30}	9.8×10^{-8}	30	-4.0	-1.9
J0218+4232[1]	430.5	7.7×10^{-20}	$3.15^{\rm d}$	1.5×10^{-27}	3.1×10^{-26}	1.7×10^{-26}	3.3×10^{-26}	1.0×10^{31}	1.3×10^{-7}	22	-3.0	-1.7
J0248+4230	384.5	1.7×10^{-20}	$1.85^{\rm b}$	1.1×10^{-27}	2.6×10^{-26}	1.8×10^{-26}	3.2×10^{-26}	7.4×10^{30}	9.5×10^{-8}	29	-3.4	-1.8
J0251+26	393.5	7.6×10^{-21}	$1.15^{\rm b}$	1.2×10^{-27}	2.0×10^{-26}	8.4×10^{-27}	1.8×10^{-26}	2.4×10^{30}	3.1×10^{-8}	15	-4.0	-2.1
J0308+74	316.8	1.7×10^{-20}	$0.38^{\rm b}$	5.0×10^{-27}	1.7×10^{-26}	6.9×10^{-27}	1.5×10^{-26}	1.0×10^{30}	1.3×10^{-8}	3	-3.9	-2.2
J0340+4130[1]	303.1	6.7×10^{-21}	$1.60^{\rm b}$	7.2×10^{-28}	2.9×10^{-26}	7.8×10^{-27}	1.7×10^{-26}	5.3×10^{30}	6.8×10^{-8}	23	-3.5	-2.1
J0348+0432[1]	25.6	2.3×10^{-19}	$2.10^{\rm e}$	9.3×10^{-28}	1.4×10^{-25}	8.8×10^{-27}	1.8×10^{-26}	1.1×10^{33}	1.4×10^{-5}	20	-4.9	-2.6
J0359+5414	12.6	1.7×10^{-14}	$\cdots$	$\cdots$	7.9×10^{-24}	4.0×10^{-26}	8.6×10^{-26}	$\cdots$	$\cdots$	$\cdots$	-4.8	-2.7
J0407+1607	38.9	7.9×10^{-20}	$1.34^{\rm b}$	1.1×10^{-27}	4.8×10^{-26}	5.3×10^{-27}	1.1×10^{-26}	1.8×10^{32}	2.4×10^{-6}	11	-4.7	-2.4
J0437−4715[1]	173.7	1.4×10^{-20}	$0.16^{\rm f}$	7.9×10^{-28}	1.5×10^{-26}	8.3×10^{-27}	1.6×10^{-26}	1.5×10^{30}	2.0×10^{-8}	2	-4.4	-2.5
J0453+1559[1]	21.8	1.8×10^{-19}	$0.52^{\rm b}$	3.1×10^{-27}	1.9×10^{-25}	9.2×10^{-27}	2.1×10^{-26}	4.1×10^{32}	5.3×10^{-6}	6.6	-5.2	-2.8
J0533+67	227.9	1.3×10^{-20}	$2.28^{\rm b}$	6.0×10^{-28}	1.4×10^{-26}	6.7×10^{-27}	1.4×10^{-26}	1.1×10^{31}	1.5×10^{-7}	24	-3.9	-2.0
J0557+1550	391.2	7.4×10^{-21}	$1.83^{\rm b}$	7.5×10^{-28}	1.7×10^{-26}	1.0×10^{-26}	2.1×10^{-26}	4.7×10^{30}	6.1×10^{-8}	29	-4.0	-2.0
J0605+37	366.6	4.7×10^{-21}	$0.19^{\rm b}$	5.6×10^{-27}	2.3×10^{-26}	1.6×10^{-26}	3.1×10^{-26}	8.0×10^{29}	1.0×10^{-8}	5.6	-3.0	-1.3
J0609+2130	18.0	2.4×10^{-19}	$0.57^{\rm b}$	2.9×10^{-27}	8.9×10^{-25}	1.9×10^{-26}	3.9×10^{-26}	1.3×10^{33}	1.6×10^{-5}	13	-4.6	-2.6
J0610−2100[1]	259.0	1.1×10^{-21}	$3.26^{\rm b}$	1.3×10^{-28}	1.7×10^{-26}	6.0×10^{-27}	1.3×10^{-26}	1.2×10^{31}	1.5×10^{-7}	99	-4.0	-2.2
J0613−0200	326.6	$8.9\times10^{-21\rm g}$	$0.78^{\rm g}$	1.8×10^{-27}	1.7×10^{-26}	1.1×10^{-26}	2.3×10^{-26}	3.1×10^{30}	4.0×10^{-8}	13	-3.9	-1.9
J0614−3329[1]	317.6	1.8×10^{-20}	$0.63^{\rm h}$	3.0×10^{-27}	2.4×10^{-26}	1.0×10^{-26}	1.9×10^{-26}	2.1×10^{30}	2.8×10^{-8}	6.2	-3.8	-2.0
J0621+1002[1]	34.7	4.6×10^{-20}	$0.42^{\rm b}$	2.4×10^{-27}	7.0×10^{-26}	7.7×10^{-27}	1.6×10^{-26}	1.0×10^{32}	1.3×10^{-6}	6.6	-4.6	-2.3
J0621+25	367.4	2.5×10^{-20}	$1.64^{\rm b}$	1.5×10^{-27}	2.6×10^{-26}	1.1×10^{-26}	2.5×10^{-26}	5.5×10^{30}	7.1×10^{-8}	17	-3.7	-1.9
J0636+5129[1]	348.6	3.4×10^{-21}	$0.21^{\rm b}$	4.2×10^{-27}	1.6×10^{-26}	6.2×10^{-27}	1.4×10^{-26}	4.5×10^{29}	5.8×10^{-9}	3.4	-4.8	-2.3
J0645+5158[1]	112.9	3.6×10^{-21}	$1.20^{\rm a}$	4.3×10^{-28}	1.7×10^{-26}	8.5×10^{-27}	1.7×10^{-26}	2.9×10^{31}	3.8×10^{-7}	39	-3.4	-1.5
J0721−2038	64.3	4.4×10^{-20}	$2.68^{\rm b}$	5.1×10^{-28}	3.2×10^{-26}	7.4×10^{-27}	1.5×10^{-26}	1.7×10^{32}	2.2×10^{-6}	29	-3.6	-1.6
J0737−3039A[1]	44.1	1.8×10^{-18}	$1.10^{\rm i}$	6.5×10^{-27}	5.1×10^{-26}	5.2×10^{-27}	1.1×10^{-26}	1.2×10^{32}	1.5×10^{-6}	1.7	-4.3	-2.3
J0740+6620[1]	346.5	8.6×10^{-21}	$0.40^{\rm a}$	3.5×10^{-27}	1.6×10^{-26}	7.9×10^{-27}	1.6×10^{-26}	9.9×10^{29}	1.3×10^{-8}	4.7	-4.9	-2.3
J0751+1807	287.5	$6.2\times10^{-21\rm g}$	$1.00^{\rm g}$	1.1×10^{-27}	1.6×10^{-26}	5.7×10^{-27}	1.3×10^{-26}	2.8×10^{30}	3.6×10^{-8}	12	-4.1	-2.2
J0900−3144	90.0	$5.0\times10^{-20\rm g}$	$0.81^{\rm g}$	2.1×10^{-27}	1.6×10^{-26}	5.0×10^{-27}	1.1×10^{-26}	2.0×10^{31}	2.6×10^{-7}	5.1	-5.0	-2.8
J0931−1902[1]	215.6	3.2×10^{-21}	$3.72^{\rm b}$	1.8×10^{-28}	1.6×10^{-26}	5.8×10^{-27}	1.3×10^{-26}	1.9×10^{31}	2.4×10^{-7}	71	-3.9	-2.1
J0952−0607	707.3	4.8×10^{-21}	$1.74^{\rm b}$	8.5×10^{-28}	5.5×10^{-26}	2.7×10^{-26}	5.5×10^{-26}	3.5×10^{30}	4.5×10^{-8}	65	-2.1	-1.1

Table 2 continued

Table 2 *(continued)*

Pulsar Name	$f_{\rm rot}$	$\dot{P}_{\rm rot}$	Distance	$h_0^{\rm sd}$	$C_{21}^{95\%}$	$C_{22}^{95\%}$	$h_0^{95\%}$	$Q_{22}^{95\%}$	$\varepsilon^{95\%}$	$h_0^{95\%}/h_0^{\rm sd}$	$\mathcal{O}_{m=1,2}^{l=2}$	$\mathcal{O}_{m=2}^{l=2}$
(J2000)	(Hz)	(s s^{-1})	(kpc)					(kg m^2)				
J0955−61	500.2	1.4×10^{-20}	2.17[b]	9.9×10^{-28}	3.8×10^{-26}	1.2×10^{-26}	2.6×10^{-26}	4.1×10^{30}	5.3×10^{-8}	26	-3.6	-2.1
J1012+5307	190.3	8.0×10^{-21}[g]	1.11[k]	9.0×10^{-28}	1.6×10^{-26}	6.5×10^{-27}	1.3×10^{-26}	7.5×10^{30}	9.7×10^{-8}	15	-3.9	-2.0
J1012−4235	322.5	6.6×10^{-21}	0.37[b]	3.2×10^{-27}	1.6×10^{-26}	8.9×10^{-27}	1.8×10^{-26}	1.2×10^{30}	1.5×10^{-8}	5.7	-3.9	-1.9
J1017−7156	427.6	1.2×10^{-21}[kk]	0.70[l]	8.3×10^{-28}	1.7×10^{-26}	8.9×10^{-27}	1.9×10^{-26}	1.3×10^{30}	1.7×10^{-8}	23	-4.2	-2.2
J1022+1001	60.8	3.0×10^{-20}[g]	1.09[g]	1.0×10^{-27}	3.5×10^{-26}	5.8×10^{-27}	1.2×10^{-26}	6.5×10^{31}	8.4×10^{-7}	12	-4.0	-2.0
J1024−0719[2]	193.7	$\cdots$	1.08[g]	$\cdots$	1.7×10^{-26}	8.5×10^{-27}	1.7×10^{-26}	9.0×10^{30}	1.2×10^{-7}	$\cdots$	-3.7	-1.9
J1035−6720[2]	348.2	$\cdots$	1.46[b]	$\cdots$	1.9×10^{-26}	6.8×10^{-27}	1.5×10^{-26}	3.2×10^{30}	4.2×10^{-8}	$\cdots$	-4.7	-2.3
J1036−8317	293.4	3.1×10^{-20}	0.93[b]	2.6×10^{-27}	2.2×10^{-26}	8.1×10^{-27}	1.7×10^{-26}	3.4×10^{30}	4.4×10^{-8}	6.6	-3.7	-2.0
J1038+0032	34.7	6.7×10^{-20}	5.94[b]	2.1×10^{-28}	6.5×10^{-26}	6.6×10^{-27}	1.4×10^{-26}	1.3×10^{33}	1.6×10^{-5}	68	-4.7	-2.4
J1055−6028	10.0	3.0×10^{-14}	3.83[b]	1.1×10^{-25}	8.4×10^{-23}	1.2×10^{-25}	2.0×10^{-25}	1.4×10^{35}	1.8×10^{-3}	1.8	-1.8	-3.0
J1124−3653	415.0	6.0×10^{-21}	1.05[b]	1.2×10^{-27}	3.1×10^{-26}	6.9×10^{-27}	1.6×10^{-26}	1.8×10^{30}	2.4×10^{-8}	14	-3.7	-2.2
J1125+7819[2]	238.0	$\cdots$	0.88[b]	$\cdots$	2.1×10^{-26}	4.7×10^{-27}	1.0×10^{-26}	2.9×10^{30}	3.7×10^{-8}	$\cdots$	-3.8	-2.2
J1125−5825	322.4	5.9×10^{-20}[kk]	1.74[b]	2.0×10^{-27}	2.0×10^{-26}	1.0×10^{-26}	2.0×10^{-26}	6.1×10^{30}	7.8×10^{-8}	9.8	-3.8	-1.9
J1137+7528	398.0	3.2×10^{-21}	3.81[b]	2.4×10^{-28}	2.4×10^{-26}	7.8×10^{-27}	1.6×10^{-26}	7.1×10^{30}	9.2×10^{-8}	67	-3.8	-2.2
J1142+0119	197.0	1.5×10^{-20}	2.18[b]	6.4×10^{-28}	3.1×10^{-26}	1.0×10^{-26}	2.4×10^{-26}	2.5×10^{31}	3.2×10^{-7}	38	-2.8	-1.3
J1207−5050	206.5	6.1×10^{-21}	1.27[b]	7.1×10^{-28}	1.5×10^{-26}	5.4×10^{-27}	1.1×10^{-26}	6.1×10^{30}	7.9×10^{-8}	16	-3.9	-2.1
J1231−1411[1]	271.5	8.2×10^{-21}	0.42[b]	2.9×10^{-27}	1.9×10^{-26}	7.9×10^{-27}	1.7×10^{-26}	1.7×10^{30}	2.3×10^{-8}	5.8	-3.7	-1.9
J1300+1240[1]	160.8	3.1×10^{-20}	0.60[m]	3.0×10^{-27}	2.3×10^{-26}	5.5×10^{-27}	1.2×10^{-26}	5.2×10^{30}	6.7×10^{-8}	4.1	-3.7	-2.1
J1301+0833	542.4	1.1×10^{-20}	1.23[b]	1.6×10^{-27}	2.7×10^{-26}	2.0×10^{-26}	4.3×10^{-26}	3.3×10^{30}	4.3×10^{-8}	28	-3.6	-1.9
J1302−32	265.2	6.6×10^{-21}	1.49[b]	7.1×10^{-28}	2.0×10^{-26}	6.2×10^{-27}	1.3×10^{-26}	4.9×10^{30}	6.3×10^{-8}	18	-3.9	-2.2
J1311−3430	390.6	2.1×10^{-20}	2.43[b]	9.5×10^{-28}	1.8×10^{-26}	1.3×10^{-26}	2.8×10^{-26}	8.0×10^{30}	1.0×10^{-7}	29	-3.7	-1.7
J1312+0051	236.5	1.8×10^{-20}	1.47[b]	1.1×10^{-27}	1.9×10^{-26}	6.8×10^{-27}	1.4×10^{-26}	6.9×10^{30}	8.9×10^{-8}	13	-3.8	-2.0
J1327−0755[2]	373.4	$\cdots$	1.70[n]	$\cdots$	1.6×10^{-26}	8.7×10^{-27}	1.8×10^{-26}	4.1×10^{30}	5.3×10^{-8}	$\cdots$	-4.0	-2.1
J1446−4701	455.6	9.7×10^{-21}[kk]	1.57[b]	1.1×10^{-27}	2.7×10^{-26}	1.4×10^{-26}	2.9×10^{-26}	4.0×10^{30}	5.2×10^{-8}	27	-3.6	-1.9
J1453+1902[1]	172.6	9.1×10^{-21}	1.27[b]	8.0×10^{-28}	1.9×10^{-26}	8.3×10^{-27}	1.6×10^{-26}	1.2×10^{31}	1.6×10^{-7}	20	-4.1	-2.4
J1455−3330	125.2	2.3×10^{-20}[g]	0.80[g]	1.7×10^{-27}	2.1×10^{-26}	5.2×10^{-27}	1.0×10^{-26}	9.5×10^{30}	1.2×10^{-7}	5.9	-3.8	-2.0
J1513−2550	471.9	2.1×10^{-20}	3.97[b]	6.5×10^{-28}	1.7×10^{-26}	8.6×10^{-27}	1.9×10^{-26}	6.2×10^{30}	8.0×10^{-8}	29	-4.3	-2.2
J1514−4946[1]	278.6	1.2×10^{-20}	0.91[b]	1.6×10^{-27}	1.4×10^{-26}	6.2×10^{-27}	1.4×10^{-26}	2.9×10^{30}	3.8×10^{-8}	8.6	-4.0	-2.1
J1518+4904[1]	24.4	2.3×10^{-20}	0.96[b]	6.3×10^{-28}	2.0×10^{-26}	8.2×10^{-27}	1.8×10^{-26}	5.2×10^{32}	6.8×10^{-6}	28	-4.8	-2.8
J1528−3146	16.4	2.5×10^{-19}	0.77[b]	2.1×10^{-27}	1.6×10^{-24}	1.8×10^{-26}	3.7×10^{-26}	1.9×10^{33}	2.5×10^{-5}	18	-4.5	-2.6
J1536−4948	324.7	2.1×10^{-20}	0.98[b]	2.2×10^{-27}	2.0×10^{-26}	8.8×10^{-27}	2.0×10^{-26}	3.5×10^{30}	4.5×10^{-8}	9.5	-3.7	-2.0
J1537+1155[1]	26.4	2.4×10^{-18}	1.05[p]	6.1×10^{-27}	1.3×10^{-25}	7.4×10^{-27}	1.6×10^{-26}	4.3×10^{32}	5.5×10^{-6}	2.6	-4.9	-2.7
J1544+4937	463.1	2.9×10^{-21}	2.99[b]	3.1×10^{-28}	1.8×10^{-26}	1.0×10^{-26}	2.2×10^{-26}	5.5×10^{30}	7.1×10^{-8}	69	-4.0	-2.1
J1551−0658	141.0	2.0×10^{-20}	1.32[b]	1.0×10^{-27}	2.4×10^{-26}	1.1×10^{-26}	2.1×10^{-26}	2.5×10^{31}	3.3×10^{-7}	20	-3.0	-1.5

Table 2 continued

Table 2 *(continued)*

Pulsar Name (J2000)	$f_{\rm rot}$ (Hz)	$\dot{P}_{\rm rot}$ (s s^{-1})	Distance (kpc)	$h_0^{\rm sd}$	$C_{21}^{95\%}$	$C_{22}^{95\%}$	$h_0^{95\%}$	$Q_{22}^{95\%}$ (kg m^2)	$\varepsilon^{95\%}$	$h_0^{95\%}/h_0^{\rm sd}$	$\mathcal{O}_{m=1,2}^{l=2}$	$\mathcal{O}_{m=2}^{l=2}$
J1552+5437	411.9	2.8×10^{-21}	2.64[b]	3.3×10^{-28}	2.7×10^{-26}	9.1×10^{-27}	1.8×10^{-26}	5.3×10^{30}	6.8×10^{-8}	56	-3.5	-2.1
J1600−3053	277.9	$8.6\times10^{-21{\rm g}}$	1.49[g]	8.4×10^{-28}	1.8×10^{-26}	6.6×10^{-27}	1.4×10^{-26}	4.9×10^{30}	6.3×10^{-8}	17	-4.0	-2.2
J1603−7202[1]	67.4	1.4×10^{-20}	0.53[f]	1.5×10^{-27}	3.3×10^{-26}	5.1×10^{-27}	1.0×10^{-26}	2.1×10^{31}	2.8×10^{-7}	6.7	-3.7	-2.1
J1614−2230[1]	317.4	3.5×10^{-21}	0.67[a]	1.3×10^{-27}	1.8×10^{-26}	1.2×10^{-26}	2.4×10^{-26}	2.9×10^{30}	3.8×10^{-8}	19	-3.4	-1.6
J1618−3921	83.4	5.4×10^{-20}	5.52[b]	3.1×10^{-28}	2.3×10^{-26}	4.2×10^{-27}	9.1×10^{-27}	1.3×10^{32}	1.7×10^{-6}	29	-4.0	-2.1
J1623−2631[3]	90.3	8.8×10^{-20}	1.80[q]	1.3×10^{-27}	2.7×10^{-26}	4.1×10^{-27}	8.9×10^{-27}	3.6×10^{31}	4.6×10^{-7}	7	-3.7	-2.1
J1623−5005	11.8	4.2×10^{-15}	...	...	1.0×10^{-23}	7.4×10^{-26}	1.5×10^{-25}	...	...	...	-3.9	-2.3
J1628−3205	311.4	1.3×10^{-20}	1.22[b]	1.3×10^{-27}	1.6×10^{-26}	8.4×10^{-27}	1.7×10^{-26}	4.0×10^{30}	5.2×10^{-8}	13	-4.0	-2.1
J1630+37	301.4	1.1×10^{-20}	1.18[b]	1.2×10^{-27}	1.6×10^{-26}	1.6×10^{-26}	3.3×10^{-26}	7.7×10^{30}	1.0×10^{-7}	27	-3.3	-1.4
J1640+2224[1]	316.1	1.3×10^{-21}	1.52[r]	3.4×10^{-28}	2.6×10^{-26}	9.9×10^{-27}	1.9×10^{-26}	5.3×10^{30}	6.9×10^{-8}	57	-3.5	-2.0
J1643−1224	216.4	$1.8\times10^{-20{\rm g}}$	0.76[g]	2.1×10^{-27}	1.8×10^{-26}	5.9×10^{-27}	1.2×10^{-26}	3.7×10^{30}	4.8×10^{-8}	5.9	-3.9	-2.1
J1653−2054	242.2	1.1×10^{-20}	2.63[b]	5.0×10^{-28}	1.5×10^{-26}	6.1×10^{-27}	1.3×10^{-26}	1.1×10^{31}	1.4×10^{-7}	26	-3.9	-2.1
J1658−5324[1]	410.0	1.1×10^{-20}	0.88[b]	1.9×10^{-27}	1.4×10^{-26}	2.4×10^{-26}	4.9×10^{-26}	4.7×10^{30}	6.0×10^{-8}	25	-2.6	-0.7
J1710+49	310.5	1.8×10^{-20}	0.51[b]	3.8×10^{-27}	2.0×10^{-26}	5.6×10^{-27}	1.2×10^{-26}	1.2×10^{30}	1.6×10^{-8}	3.3	-4.1	-2.3
J1713+0747	218.8	$8.1\times10^{-21{\rm g}}$	1.11[g]	9.7×10^{-28}	1.8×10^{-26}	8.4×10^{-27}	1.7×10^{-26}	7.0×10^{30}	9.1×10^{-8}	17	-3.5	-1.8
J1719−1438[2]	172.7	...	0.34[b]	...	1.7×10^{-26}	7.4×10^{-27}	1.5×10^{-26}	3.1×10^{30}	4.0×10^{-8}	...	-4.3	-2.5
J1721−2457[2]	286.0	...	1.37[b]	...	1.6×10^{-26}	7.2×10^{-27}	1.5×10^{-26}	4.7×10^{30}	6.0×10^{-8}	...	-4.0	-2.1
J1727−2946[1]	36.9	2.4×10^{-19}	1.88[b]	1.3×10^{-27}	1.0×10^{-25}	8.0×10^{-27}	1.8×10^{-26}	4.6×10^{32}	5.9×10^{-6}	14	-4.0	-2.2
J1729−2117	15.1	1.7×10^{-19}	0.97[b]	1.3×10^{-27}	2.0×10^{-24}	3.7×10^{-26}	7.6×10^{-26}	5.9×10^{33}	7.7×10^{-5}	57	-4.1	-2.1
J1730−2304	123.1	$1.0\times10^{-20{\rm g}}$	0.90[g]	9.9×10^{-28}	2.0×10^{-26}	4.4×10^{-27}	9.3×10^{-27}	1.0×10^{31}	1.3×10^{-7}	9.4	-3.8	-2.1
J1732−5049[1]	188.2	1.2×10^{-20}	4.22[s]	2.8×10^{-28}	1.4×10^{-26}	5.0×10^{-27}	1.1×10^{-26}	2.3×10^{31}	3.0×10^{-7}	37	-4.1	-2.2
J1738+0333[1]	170.9	$2.2\times10^{-20{\rm t}}$	1.47[t]	1.1×10^{-27}	1.5×10^{-26}	4.8×10^{-27}	1.0×10^{-26}	9.3×10^{30}	1.2×10^{-7}	9.5	-4.6	-2.7
J1741+1351[1]	266.9	2.9×10^{-20}	1.08[u]	2.1×10^{-27}	2.0×10^{-26}	1.1×10^{-26}	2.2×10^{-26}	6.0×10^{30}	7.8×10^{-8}	11	-3.3	-1.5
J1744−1134	245.4	$7.0\times10^{-21{\rm g}}$	0.42[g]	2.5×10^{-27}	2.1×10^{-26}	1.3×10^{-26}	2.5×10^{-26}	3.2×10^{30}	4.1×10^{-8}	10	-2.7	-1.1
J1744−7619[2]	213.3	...	...	...	1.3×10^{-26}	6.6×10^{-27}	1.4×10^{-26}	...	...	...	-4.0	-2.0
J1745+1017[1]	377.1	2.2×10^{-21}	1.21[b]	6.0×10^{-28}	1.6×10^{-26}	7.4×10^{-27}	1.6×10^{-26}	2.5×10^{30}	3.3×10^{-8}	27	-4.1	-2.3
J1747−4036[1]	607.7	1.1×10^{-20}	7.15[b]	2.9×10^{-28}	2.9×10^{-26}	1.2×10^{-26}	2.6×10^{-26}	9.3×10^{30}	1.2×10^{-7}	90	-3.9	-2.1
J1748−2446A[3]	86.5	9.2×10^{-20}	5.50[v]	4.1×10^{-28}	2.1×10^{-26}	6.9×10^{-27}	1.4×10^{-26}	1.8×10^{32}	2.4×10^{-6}	33	-3.8	-1.8
J1748−30[2]	103.3	...	13.81[b]	...	3.5×10^{-26}	6.6×10^{-27}	1.4×10^{-26}	3.3×10^{32}	4.3×10^{-6}	...	-3.0	-1.8
J1750−2536	28.8	8.1×10^{-20}	3.22[b]	3.8×10^{-28}	1.2×10^{-26}	1.1×10^{-26}	2.0×10^{-26}	1.4×10^{33}	1.8×10^{-5}	52	-4.6	-2.4
J1751−2857[1]	255.4	1.0×10^{-20}	1.09[b]	1.2×10^{-27}	1.5×10^{-26}	8.5×10^{-27}	1.8×10^{-26}	5.5×10^{30}	7.2×10^{-8}	15	-3.8	-2.0
J1753−1914	15.9	2.0×10^{-18}	2.91[b]	1.6×10^{-27}	1.9×10^{-24}	2.3×10^{-26}	4.7×10^{-26}	9.9×10^{33}	1.3×10^{-4}	30	-4.5	-2.7
J1753−2240	10.5	9.7×10^{-19}	3.23[b]	8.0×10^{-28}	2.2×10^{-23}	1.6×10^{-25}	3.2×10^{-25}	1.7×10^{35}	2.2×10^{-3}	410	-4.0	-2.2
J1756−2251[1]	35.1	1.0×10^{-18}	0.73[w]	6.6×10^{-27}	5.7×10^{-26}	7.1×10^{-27}	1.5×10^{-26}	1.6×10^{32}	2.1×10^{-6}	2.3	-4.8	-2.3

Table 2 continued

Table 2 *(continued)*

Pulsar Name	$f_{\rm rot}$	$\dot{P}_{\rm rot}$	Distance	$h_0^{\rm sd}$	$C_{21}^{95\%}$	$C_{22}^{95\%}$	$h_0^{95\%}$	$Q_{22}^{95\%}$	$\varepsilon^{95\%}$	$h_0^{95\%}/h_0^{\rm sd}$	$\mathcal{O}_{m=1,2}^{l=2}$	$\mathcal{O}_{m=2}^{l=2}$
(J2000)	(Hz)	(s s^{-1})	(kpc)					(kg m^2)				
J1757−27	56.5	2.1×10^{-19}	8.12[b]	3.4×10^{-28}	3.4×10^{-26}	7.2×10^{-27}	1.4×10^{-26}	6.3×10^{32}	8.2×10^{-6}	40	-4.1	-2.0
J1801−1417[1]	275.9	3.8×10^{-21}	1.10[b]	7.5×10^{-28}	2.0×10^{-26}	8.1×10^{-27}	1.8×10^{-26}	4.7×10^{30}	6.1×10^{-8}	24	-3.7	-1.9
J1801−3210[2]	134.2	⋯	6.12[b]	⋯	1.3×10^{-26}	4.1×10^{-27}	9.0×10^{-27}	5.6×10^{31}	7.2×10^{-7}	⋯	-4.1	-2.1
J1802−2124	79.1	7.2×10^{-20}[g]	0.64[g]	3.0×10^{-27}	2.5×10^{-26}	4.4×10^{-27}	9.4×10^{-27}	1.8×10^{31}	2.3×10^{-7}	3.1	-4.0	-2.1
J1804−0735[3]	43.3	1.8×10^{-19}	7.80[x]	2.9×10^{-28}	4.4×10^{-26}	6.4×10^{-27}	1.3×10^{-26}	1.0×10^{33}	1.3×10^{-5}	45	-4.7	-2.3
J1804−2717[1]	107.0	3.5×10^{-20}	0.80[b]	1.9×10^{-27}	1.8×10^{-26}	4.7×10^{-27}	9.8×10^{-27}	1.2×10^{31}	1.6×10^{-7}	5	-3.8	-2.0
J1807−2459A[3]	326.9	2.4×10^{-20}	2.79[y]	8.1×10^{-28}	1.8×10^{-26}	2.1×10^{-26}	4.2×10^{-26}	2.0×10^{31}	2.6×10^{-7}	52	-2.5	-0.5
J1810+1744	601.4	4.5×10^{-21}	2.36[b]	5.6×10^{-28}	2.0×10^{-26}	1.6×10^{-26}	3.5×10^{-26}	4.2×10^{30}	5.4×10^{-8}	63	-4.0	-1.9
J1810−2005[1]	30.5	5.3×10^{-20}	3.51[b]	2.9×10^{-28}	2.0×10^{-25}	6.3×10^{-27}	1.6×10^{-26}	1.1×10^{33}	1.5×10^{-5}	56	-3.9	-2.6
J1811−2405	375.9	1.3×10^{-20}[kk]	1.83[b]	9.7×10^{-28}	2.0×10^{-26}	1.0×10^{-26}	2.1×10^{-26}	4.9×10^{30}	6.3×10^{-8}	21	-3.9	-2.1
J1813−2621[2]	225.7	⋯	3.01[b]	⋯	1.6×10^{-26}	5.1×10^{-27}	1.1×10^{-26}	1.2×10^{31}	1.5×10^{-7}	⋯	-4.0	-2.1
J1816+4510[1]	313.2	4.3×10^{-20}	4.36[b]	6.8×10^{-28}	1.9×10^{-26}	7.0×10^{-27}	1.4×10^{-26}	1.1×10^{31}	1.5×10^{-7}	21	-3.9	-2.1
J1823−3021A	183.8	3.4×10^{-18}	8.40[aa]	2.4×10^{-27}	2.7×10^{-26}	9.7×10^{-27}	2.0×10^{-26}	9.3×10^{31}	1.2×10^{-6}	8.6	-2.6	-1.1
J1824−2452A	327.4	1.6×10^{-18}	5.10[bb]	3.6×10^{-27}	2.3×10^{-26}	1.0×10^{-26}	2.0×10^{-26}	1.7×10^{31}	2.3×10^{-7}	5.5	-3.9	-2.0
J1825−0319	219.6	6.8×10^{-21}	3.86[b]	2.6×10^{-28}	2.3×10^{-26}	7.9×10^{-27}	1.5×10^{-26}	2.2×10^{31}	2.9×10^{-7}	60	-3.5	-1.9
J1827−0849	445.9	1.1×10^{-20}	⋯	⋯	2.2×10^{-26}	9.6×10^{-27}	2.1×10^{-26}	⋯	⋯	⋯	-4.0	-2.2
J1832−0836[2]	367.8	⋯	2.50[a]	⋯	2.2×10^{-26}	6.9×10^{-27}	1.4×10^{-26}	4.8×10^{30}	6.3×10^{-8}	⋯	-4.1	-2.3
J1840−0643	28.1	2.2×10^{-16}	5.01[b]	1.3×10^{-26}	9.1×10^{-26}	1.8×10^{-26}	3.5×10^{-26}	4.0×10^{33}	5.2×10^{-5}	2.8	-3.5	-1.2
J1841+0130	33.6	8.2×10^{-18}	4.23[b]	3.2×10^{-27}	7.3×10^{-26}	6.4×10^{-27}	1.4×10^{-26}	9.6×10^{32}	1.2×10^{-5}	4.4	-4.6	-2.4
J1843−1113	541.8	9.4×10^{-21}[g]	1.48[s]	1.2×10^{-27}	2.2×10^{-26}	2.2×10^{-26}	4.6×10^{-26}	4.2×10^{30}	5.5×10^{-8}	37	-3.6	-1.6
J1844+0115	238.9	1.1×10^{-20}	4.36[b]	3.0×10^{-28}	1.4×10^{-26}	6.2×10^{-27}	1.3×10^{-26}	1.9×10^{31}	2.4×10^{-7}	45	-4.0	-2.1
J1850+0124	280.9	1.1×10^{-20}	3.39[b]	4.2×10^{-28}	1.8×10^{-26}	7.5×10^{-27}	1.6×10^{-26}	1.3×10^{31}	1.6×10^{-7}	39	-3.8	-2.1
J1853+1303[1]	244.4	8.7×10^{-21}	1.32[b]	8.9×10^{-28}	2.5×10^{-26}	9.8×10^{-27}	2.2×10^{-26}	8.9×10^{30}	1.1×10^{-7}	25	-3.4	-1.8
J1855−1436	278.2	1.1×10^{-20}	5.15[b]	2.7×10^{-28}	2.3×10^{-26}	1.0×10^{-26}	2.0×10^{-26}	2.5×10^{31}	3.2×10^{-7}	74	-3.4	-1.8
J1857+0943	186.5	1.7×10^{-20}[g]	1.10[g]	1.3×10^{-27}	1.3×10^{-26}	4.5×10^{-27}	1.0×10^{-26}	5.8×10^{30}	7.6×10^{-8}	7.7	-4.2	-2.2
J1858−2216	419.5	3.9×10^{-21}	0.92[b]	1.1×10^{-27}	2.4×10^{-26}	8.7×10^{-27}	1.9×10^{-26}	1.8×10^{30}	2.4×10^{-7}	17	-3.8	-2.1
J1900+0308	203.7	5.9×10^{-21}	4.80[b]	1.8×10^{-28}	2.1×10^{-26}	5.0×10^{-27}	1.1×10^{-26}	2.3×10^{31}	2.9×10^{-7}	58	-3.8	-2.2
J1902−5105[1]	573.9	8.7×10^{-21}	1.65[b]	1.1×10^{-27}	2.1×10^{-26}	1.4×10^{-26}	2.9×10^{-26}	2.7×10^{30}	3.5×10^{-8}	27	-4.1	-2.1
J1903+0327[1]	465.1	2.0×10^{-20}	6.11[b]	4.0×10^{-28}	2.5×10^{-26}	9.7×10^{-27}	2.1×10^{-26}	1.1×10^{31}	1.4×10^{-7}	52	-3.9	-2.1
J1903−7051[1]	277.9	7.7×10^{-21}	0.93[b]	1.3×10^{-27}	2.0×10^{-26}	7.2×10^{-27}	1.6×10^{-26}	3.5×10^{30}	4.5×10^{-8}	13	-3.7	-2.0
J1904+0412	14.1	1.1×10^{-19}	4.58[b]	2.2×10^{-28}	3.6×10^{-24}	4.3×10^{-26}	7.9×10^{-26}	3.3×10^{34}	4.3×10^{-4}	360	-4.3	-2.3
J1904+0451	164.1	5.7×10^{-21}	4.40[b]	1.8×10^{-28}	1.5×10^{-26}	4.9×10^{-27}	1.1×10^{-26}	3.2×10^{31}	4.1×10^{-7}	60	-4.2	-2.3
J1905+0400[1]	264.2	4.2×10^{-21}	1.06[b]	8.0×10^{-28}	1.4×10^{-26}	8.3×10^{-27}	1.8×10^{-26}	4.9×10^{30}	6.4×10^{-8}	22	-3.9	-1.9
J1908+2105	390.0	1.4×10^{-20}	2.58[b]	7.3×10^{-28}	2.5×10^{-26}	1.3×10^{-26}	2.5×10^{-26}	7.7×10^{30}	9.9×10^{-8}	34	-3.4	-1.9

Table 2 continued

Table 2 (*continued*)

Pulsar Name (J2000)	f_rot (Hz)	$\dot{P}_\mathrm{rot}$ (s s^{-1})	Distance (kpc)	h_0^sd	$C_{21}^{95\%}$	$C_{22}^{95\%}$	$h_0^{95\%}$	$Q_{22}^{95\%}$ (kg m^2)	$\varepsilon^{95\%}$	$h_0^{95\%}/h_0^\mathrm{sd}$	$\mathcal{O}_{m=1,2}^{l=2}$	$\mathcal{O}_{m=2}^{l=2}$
J1909−3744	339.3	2.7×10^{-21}g	1.15$^\mathrm{g}$	6.7×10^{-28}	2.5×10^{-26}	1.6×10^{-26}	3.2×10^{-26}	5.8×10^{30}	7.5×10^{-8}	47	-3.1	-1.3
J1910+1256	200.7	9.3×10^{-21}g	1.16$^\mathrm{s}$	9.5×10^{-28}	2.5×10^{-26}	5.5×10^{-27}	1.2×10^{-26}	6.4×10^{30}	8.3×10^{-8}	13	-3.5	-2.1
J1910−5959A[3]	306.2	2.6×10^{-20}	4.50$^\mathrm{ee}$	5.0×10^{-28}	1.9×10^{-26}	6.3×10^{-27}	1.4×10^{-26}	1.2×10^{31}	1.6×10^{-7}	27	-4.1	-2.2
J1910−5959C[3]	189.5	4.2×10^{-20}	4.50$^\mathrm{ee}$	5.0×10^{-28}	1.6×10^{-26}	4.9×10^{-27}	1.1×10^{-26}	2.4×10^{31}	3.1×10^{-7}	21	-3.9	-2.2
J1910−5959D[3]	110.7	7.2×10^{-20}	4.50$^\mathrm{ee}$	5.0×10^{-28}	2.2×10^{-26}	5.3×10^{-27}	1.2×10^{-26}	7.7×10^{31}	1.0×10^{-6}	23	-3.4	-1.9
J1911+1347[1]	216.2	1.7×10^{-20}	1.36$^\mathrm{b}$	1.1×10^{-27}	1.5×10^{-26}	5.2×10^{-27}	1.2×10^{-26}	6.1×10^{30}	7.9×10^{-8}	10	-4.0	-2.1
J1911−1114[1]	275.8	1.1×10^{-20}	1.07$^\mathrm{b}$	1.3×10^{-27}	1.7×10^{-26}	1.1×10^{-26}	2.2×10^{-26}	5.6×10^{30}	7.2×10^{-8}	16	-3.5	-1.6
J1914+0659	54.0	3.1×10^{-20}	8.47$^\mathrm{b}$	1.2×10^{-28}	2.7×10^{-26}	4.3×10^{-27}	9.1×10^{-27}	4.8×10^{32}	6.2×10^{-6}	74	-4.7	-2.2
J1915+1606[1]	16.9	8.6×10^{-18}	5.25$^\mathrm{b}$	1.9×10^{-27}	1.2×10^{-24}	1.6×10^{-26}	3.1×10^{-26}	1.0×10^{34}	1.4×10^{-4}	17	-5.8	-2.7
J1918−0642[1]	130.8	2.4×10^{-20}	1.10$^\mathrm{a}$	1.3×10^{-27}	1.9×10^{-26}	7.0×10^{-27}	1.5×10^{-26}	1.7×10^{31}	2.2×10^{-7}	11	-3.6	-1.7
J1921+0137	400.6	1.9×10^{-20}	5.06$^\mathrm{b}$	4.4×10^{-28}	4.1×10^{-26}	9.1×10^{-27}	1.7×10^{-26}	1.0×10^{31}	1.3×10^{-7}	40	-2.9	-2.1
J1923+2515[1]	264.0	7.0×10^{-21}	1.20$^\mathrm{b}$	9.1×10^{-28}	1.9×10^{-26}	5.7×10^{-27}	1.3×10^{-26}	4.0×10^{30}	5.1×10^{-8}	14	-4.0	-2.2
J1932+17	23.9	4.1×10^{-19}	2.07$^\mathrm{b}$	1.2×10^{-27}	2.1×10^{-25}	2.0×10^{-26}	4.0×10^{-26}	2.6×10^{33}	3.4×10^{-5}	32	-4.0	-2.0
J1939+2134	641.9	1.1×10^{-19}g	3.27$^\mathrm{g}$	2.0×10^{-27}	2.7×10^{-26}	2.3×10^{-26}	4.6×10^{-26}	6.6×10^{30}	8.6×10^{-8}	23	-3.3	-1.4
J1943+2210	196.7	8.8×10^{-21}	6.78$^\mathrm{b}$	1.6×10^{-28}	1.8×10^{-26}	6.3×10^{-27}	1.4×10^{-26}	4.3×10^{31}	5.6×10^{-7}	86	-3.8	-2.0
J1944+0907[1]	192.9	3.8×10^{-21}	1.22$^\mathrm{b}$	5.7×10^{-28}	2.2×10^{-26}	1.2×10^{-26}	2.2×10^{-26}	1.3×10^{31}	1.7×10^{-7}	38	-2.7	-1.3
J1946+3417[2]	315.4	…	6.97$^\mathrm{b}$	…	2.0×10^{-26}	6.4×10^{-27}	1.4×10^{-26}	1.8×10^{31}	2.3×10^{-7}	…	-4.0	-2.1
J1946−5403	368.9	2.7×10^{-21}	1.15$^\mathrm{b}$	7.0×10^{-28}	1.9×10^{-26}	7.8×10^{-27}	1.7×10^{-26}	2.6×10^{30}	3.4×10^{-8}	24	-4.0	-2.1
J1950+2414	232.3	1.9×10^{-20}	7.27$^\mathrm{b}$	2.3×10^{-28}	1.6×10^{-26}	9.7×10^{-27}	1.9×10^{-26}	4.8×10^{31}	6.2×10^{-7}	83	-3.5	-1.6
J1955+2527[1]	205.2	1.1×10^{-20}	8.18$^\mathrm{b}$	1.5×10^{-28}	1.7×10^{-26}	8.1×10^{-27}	1.7×10^{-26}	5.9×10^{31}	7.6×10^{-7}	110	-3.5	-1.8
J1955+2908[1]	163.0	3.1×10^{-20}	6.30$^\mathrm{b}$	2.9×10^{-28}	2.1×10^{-26}	5.9×10^{-27}	1.3×10^{-26}	5.7×10^{31}	7.4×10^{-7}	46	-3.7	-2.1
J1959+2048[1]	622.1	1.1×10^{-20}	1.73$^\mathrm{b}$	1.2×10^{-27}	2.8×10^{-26}	1.2×10^{-26}	2.5×10^{-26}	2.1×10^{30}	2.7×10^{-8}	21	-4.1	-2.2
J2007+2722	40.8	9.6×10^{-19}	7.10$^\mathrm{b}$	7.1×10^{-28}	5.7×10^{-27}	1.2×10^{-26}	2.2×10^{-26}	1.7×10^{33}	2.2×10^{-5}	30	-3.7	-1.5
J2010−1323[1]	191.5	4.0×10^{-21}	1.16$^\mathrm{b}$	6.1×10^{-28}	3.0×10^{-26}	9.1×10^{-27}	2.1×10^{-26}	1.2×10^{31}	1.6×10^{-7}	34	-2.9	-1.7
J2017+0603[1]	345.3	8.0×10^{-21}	1.40$^\mathrm{b}$	9.6×10^{-28}	2.4×10^{-26}	1.3×10^{-26}	2.7×10^{-26}	5.8×10^{30}	7.5×10^{-8}	28	-4.0	-1.6
J2017−1614	432.1	2.4×10^{-21}	1.44$^\mathrm{b}$	5.7×10^{-28}	1.7×10^{-26}	1.4×10^{-26}	3.0×10^{-26}	4.2×10^{30}	5.4×10^{-8}	52	-3.7	-1.7
J2019+2425[1]	254.2	1.6×10^{-21}	1.16$^\mathrm{b}$	4.4×10^{-28}	2.8×10^{-26}	1.4×10^{-26}	3.3×10^{-26}	1.1×10^{31}	1.4×10^{-7}	75	-3.3	-1.7
J2033+1734[1]	168.1	8.4×10^{-21}	1.74$^\mathrm{b}$	5.5×10^{-28}	1.4×10^{-26}	7.8×10^{-27}	1.6×10^{-26}	1.8×10^{31}	2.3×10^{-7}	28	-3.9	-2.0
J2042+0246	220.6	1.4×10^{-20}	0.64$^\mathrm{b}$	2.2×10^{-27}	2.1×10^{-26}	6.9×10^{-27}	1.4×10^{-26}	3.3×10^{30}	4.2×10^{-8}	6.1	-3.6	-2.0
J2043+1711[1]	420.2	4.1×10^{-21}	1.60$^\mathrm{a}$	6.6×10^{-28}	2.6×10^{-26}	1.1×10^{-26}	2.2×10^{-26}	3.7×10^{30}	4.8×10^{-8}	34	-3.9	-2.1
J2045+3633[1]	31.6	6.0×10^{-19}	5.63$^\mathrm{b}$	6.2×10^{-28}	5.3×10^{-26}	9.9×10^{-27}	2.1×10^{-26}	2.1×10^{33}	2.8×10^{-5}	33	-4.8	-2.3
J2047+1053	233.3	2.1×10^{-20}	2.79$^\mathrm{b}$	6.4×10^{-28}	3.4×10^{-26}	6.1×10^{-27}	1.3×10^{-26}	1.3×10^{31}	1.6×10^{-7}	21	-3.1	-2.1
J2051−0827[1]	221.8	1.2×10^{-20}	1.47$^\mathrm{b}$	9.0×10^{-28}	1.9×10^{-26}	8.4×10^{-27}	1.7×10^{-26}	9.4×10^{30}	1.2×10^{-7}	19	-3.6	-1.8
J2052+1218	503.7	6.7×10^{-21}	3.92$^\mathrm{b}$	3.8×10^{-28}	2.0×10^{-26}	9.6×10^{-27}	2.1×10^{-26}	6.0×10^{30}	7.7×10^{-8}	56	-4.1	-2.3

Table 2 continued

Table 2 *(continued)*

Pulsar Name (J2000)	$f_{\rm rot}$ (Hz)	$\dot{P}_{\rm rot}$ (s s^{-1})	Distance (kpc)	$h_0^{\rm sd}$	$C_{21}^{95\%}$	$C_{22}^{95\%}$	$h_0^{95\%}$	$Q_{22}^{95\%}$ (kg m^2)	$\varepsilon^{95\%}$	$h_0^{95\%}/h_0^{\rm sd}$	$\mathcal{O}_{m=1,2}^{l=2}$	$\mathcal{O}_{m=2}^{l=2}$
J2053+4650[1]	79.5	1.7×10^{-19}	$3.81^{\rm b}$	7.8×10^{-28}	1.9×10^{-26}	5.4×10^{-27}	1.1×10^{-26}	1.3×10^{32}	1.6×10^{-6}	15	-4.1	-1.9
J2129+1210A[3]	9.0	8.8×10^{-19}	$10.00^{\rm ff}$	2.3×10^{-28}	...	...	7.2×10^{-25}	1.6×10^{36}	2.1×10^{-2}	3200	-2.5	-1.9
J2129+1210B[3]	17.8	4.4×10^{-19}	$10.00^{\rm ff}$	2.3×10^{-28}	8.9×10^{-25}	1.4×10^{-26}	2.9×10^{-26}	1.7×10^{34}	2.2×10^{-4}	130	-4.9	-2.9
J2129+1210C[3]	32.8	2.4×10^{-19}	$10.00^{\rm ff}$	2.3×10^{-28}	7.2×10^{-26}	8.5×10^{-27}	1.7×10^{-26}	2.9×10^{33}	3.7×10^{-5}	75	-4.8	-2.4
J2129+1210D[3]	208.2	3.8×10^{-20}	$10.00^{\rm ff}$	2.3×10^{-28}	1.7×10^{-26}	8.5×10^{-27}	1.8×10^{-26}	7.5×10^{31}	9.7×10^{-7}	78	-3.6	-1.9
J2129+1210E[3]	215.0	3.7×10^{-20}	$10.00^{\rm ff}$	2.3×10^{-28}	1.9×10^{-26}	7.2×10^{-27}	1.5×10^{-26}	5.9×10^{31}	7.6×10^{-7}	66	-3.8	-2.0
J2145−0750	62.3	$2.9\times10^{-20\rm g}$	$0.65^{\rm g}$	1.7×10^{-27}	2.7×10^{-26}	6.9×10^{-27}	1.4×10^{-26}	4.4×10^{31}	5.7×10^{-7}	8.7	-4.1	-1.8
J2205+60	414.0	2.0×10^{-20}	$3.53^{\rm b}$	6.5×10^{-28}	1.8×10^{-26}	1.1×10^{-26}	2.4×10^{-26}	8.9×10^{30}	1.2×10^{-7}	36	-4.0	-1.9
J2214+3000[1]	320.6	1.3×10^{-20}	$0.60^{\rm a}$	2.7×10^{-27}	2.0×10^{-26}	1.3×10^{-26}	2.6×10^{-26}	2.8×10^{30}	3.6×10^{-8}	9.5	-3.5	-1.7
J2222−0137	30.5	$4.1\times10^{-21\rm gg}$	$0.27^{\rm gg}$	1.1×10^{-27}	8.6×10^{-26}	1.1×10^{-26}	2.2×10^{-26}	1.1×10^{32}	1.5×10^{-6}	20	-4.7	-2.3
J2229+2643[1]	335.8	1.4×10^{-21}	$1.80^{\rm b}$	3.1×10^{-28}	3.2×10^{-26}	1.1×10^{-26}	2.3×10^{-26}	6.6×10^{30}	8.5×10^{-8}	72	-3.2	-1.8
J2234+0611[1]	279.6	3.6×10^{-21}	$1.50^{\rm a}$	5.4×10^{-28}	2.0×10^{-26}	8.9×10^{-27}	1.8×10^{-26}	6.4×10^{30}	8.3×10^{-8}	34	-3.7	-1.9
J2234+0944[1]	275.7	1.3×10^{-20}	$0.80^{\rm a}$	1.9×10^{-27}	1.7×10^{-26}	7.7×10^{-27}	1.6×10^{-26}	3.1×10^{30}	4.0×10^{-8}	8.2	-3.9	-2.0
J2235+1506[1]	16.7	9.2×10^{-20}	$1.54^{\rm b}$	6.5×10^{-28}	1.5×10^{-24}	3.3×10^{-26}	6.2×10^{-26}	6.2×10^{33}	8.0×10^{-5}	95	-3.4	-1.9
J2241−5236	457.3	6.6×10^{-21}	$0.96^{\rm b}$	1.5×10^{-27}	2.5×10^{-26}	8.8×10^{-27}	2.0×10^{-26}	1.6×10^{30}	2.1×10^{-8}	13	-4.1	-2.2
J2256−1024	435.8	1.1×10^{-20}	$1.33^{\rm b}$	1.3×10^{-27}	2.6×10^{-26}	1.2×10^{-26}	2.3×10^{-26}	2.9×10^{30}	3.8×10^{-8}	17	-3.7	-2.1
J2310−0555	382.8	5.0×10^{-21}	$1.55^{\rm b}$	7.2×10^{-28}	1.9×10^{-26}	9.7×10^{-27}	2.0×10^{-26}	3.9×10^{30}	5.0×10^{-8}	28	-4.0	-2.1
J2317+1439	290.3	$3.5\times10^{-21\rm g}$	$1.01^{\rm g}$	8.0×10^{-28}	1.5×10^{-26}	1.2×10^{-26}	2.6×10^{-26}	5.6×10^{30}	7.2×10^{-8}	32	-3.6	-1.6
J2322+2057	208.0	$4.4\times10^{-22\rm ii}$	$0.23^{\rm ii}$	1.1×10^{-27}	2.1×10^{-26}	6.2×10^{-27}	1.3×10^{-26}	1.3×10^{30}	1.6×10^{-8}	12	-3.7	-2.0
J2339−0533[1]	346.7	6.9×10^{-21}	$1.10^{\rm jj}$	1.1×10^{-27}	2.2×10^{-26}	8.1×10^{-27}	1.8×10^{-26}	2.9×10^{30}	3.8×10^{-8}	15	-4.9	-2.4

References—The following is a list of references for pulsar distances and intrinsic period derivatives, and they should be consulted for information on the associated uncertainties on these quantities: (a) Arzoumanian et al. (2018), (b) Yao et al. (2017), (c) Kothes (2013), (d) Verbiest & Lorimer (2014), (e) Antoniadis et al. (2013), (f) Reardon et al. (2016), (g) Desvignes et al. (2016), (h) Bassa et al. (2016), (i) Deller et al. (2009), (j) Dodson et al. (2003), (k) Mingarelli, private communication, (l) Abbott et al. (2017a), (m) Verbiest et al. (2012), (n) Boyles et al. (2013), (o) Halpern et al. (2013), (p) Fonseca et al. (2014), (q) Braga et al. (2015), (r) Vigeland et al. (2018), (s) Mingarelli et al. (2018), (t) Freire et al. (2012), (u) Espinoza et al. (2013), (v) Ortolani et al. (2007), (w) Ferdman et al. (2014), (x) Harris (1996), (y) Valenti et al. (2010), (z) Marelli et al. (2014), (aa) Valenti et al. (2007), (bb) Rees & Cudworth (1991), (cc) Wang (2011), (dd) Gotthelf et al. (2011), (ee) Gratton et al. (2003), (ff) McNamara et al. (2004), (gg) Deller et al. (2013), (hh) Halpern et al. (2001), (ii) Spiewak et al. (2018), (jj) Romani & Shaw (2011), (kk) Ng et al. (2014).

[1] The observed $\dot{P}$ has been corrected to account for the relative motion between the pulsar and observer.

[2] The corrected pulsar $\dot{P}$ value is negative, so no value is given and no spin-down limit has been calculated.

[3] This is a globular cluster pulsar for which a proxy period derivative has been derived assuming a characteristic age of 10^9 years and a braking index of $n = 5$.

4. DISCUSSION

In this paper we have used data from the first two observation runs of Advanced LIGO (O1 and O2) to update the upper limits on the gravitational-wave amplitude h_0 for emission from the $l = m = 2$ mass quadrupole for 167 pulsars. This compares to 271 results presented previously in Aasi et al. (2014) (using data from the *initial* runs of the LIGO (Abbott et al. 2009) and Virgo (Accadia et al. 2012) detectors, S1–6 and VSR1–4) and Abbott et al. (2017a) (using data from the first observing run, O1, of the advanced LIGO detectors Aasi et al. 2015b; Abbott et al. 2016). New upper limits on h_0 have been set for a further 55 pulsars. Other than the results in Pitkin et al. (2015), we have also presented the first comprehensive set of results for searches that also include the possibility of emission from the $l = 2$, $m = 1$ mode at the pulsar's rotation frequency. These are expressed as upper limits on two amplitude parameters C_{21} and C_{22} defined in Jones (2015). We find no strong evidence for gravitational-wave emission from any pulsar in the searches purely for the $l = m = 2$ mode, or both the $l = 2$, $m = 1, 2$ modes.

Further analyses of this dataset are possible. For example, we have not presented any updated results regarding potential emission from non-tensorial polarization modes as performed in Abbott et al. (2018a). In addition to this, the results from all pulsars could be combined in a way, such as that described in Pitkin et al. (2018), to constrain the underlying pulsar ellipticity distribution and determine if the ensemble of all pulsar provides evidence for any gravitational-wave signal.

With the MSPs PSR J0636+5129 and J0711−6830 within a factor of ~ 3 of their respective spin-down limits, the imminent third observing run of the advanced LIGO and Virgo detectors (O3) could allow us to surpass the spin-down limit for an MSP for the first time. This offers the intriguing possibility for signal detection from these extremely smooth objects, with spin-down derived ellipticities of a few 10^{-9}. The O3 sensitivity could also bring the limits for the Crab pulsar into the range of mass quadrupoles allowed by reasonably standard neutron star equations of state.

Software: Much of the analysis described in the paper was performed using the publicly available LALSUITE library (LIGO Scientific Collaboration 2018). Production of many of the pulsar timing ephemerides used in this analysis were performed with TEMPO[11] and TEMPO2 (Hobbs et al. 2006). Figures in this publication have be produced using Matplotlib (Hunter 2007).

Facilities: Arecibo, Fermi, LIGO, Lovell, Molonglo Observatory, MtPO:26m, NICER, NRT, Parkes

APPENDIX

A. DEFINITIONS

Here we will define some of the standard useful quantities reported and used in our results (many of these are defined in Aasi et al. 2014). The standard definition for the gravitational-wave amplitude from the $l = m = 2$ mass quadrupole for a non-precessing triaxial star rotating about a principal axis, is

$$h_0 = \frac{16\pi^2 G}{c^4} \frac{I_{zz}^{\text{fid}} \varepsilon f_{\text{rot}}^2}{d} \approx 4.23 \times 10^{-26} \left(\frac{1\,\text{kpc}}{d}\right) \left(\frac{I_{zz}^{\text{fid}}}{10^{38}\,\text{kg m}^2}\right) \left(\frac{\varepsilon}{10^{-6}}\right) \left(\frac{f_{\text{rot}}}{100\,\text{Hz}}\right)^2, \tag{A1}$$

where d is the pulsar distance, I_{zz}^{fid} is the fiducial component of the moment of inertia tensor ellipsoid about the rotation axis, f_{rot} is the pulsar's rotation frequency, and ε is the star's fiducial ellipticity (see, e.g., Johnson-McDaniel 2013) defined as

$$\varepsilon = \frac{|I_{xx} - I_{yy}|}{I_{zz}^{\text{fid}}}, \tag{A2}$$

where I_{xx} and I_{yy} are the true moments of inertia about the principal axes other than the rotation axis.

The gravitational-wave amplitude is related to the $l = m = 2$ mass quadrupole Q_{22} via

$$Q_{22} \equiv I_{zz}^{\text{fid}} \varepsilon \sqrt{\frac{15}{8\pi}} = h_0 \left(\frac{c^4 d}{16\pi^2 G f_{\text{rot}}^2}\right) \sqrt{\frac{15}{8\pi}} \approx 1.83 \times 10^{32} \left(\frac{h_0}{10^{-25}}\right) \left(\frac{d}{1\,\text{kpc}}\right) \left(\frac{100\,\text{Hz}}{f_{\text{rot}}}\right)^2 \text{kg m}^2, \tag{A3}$$

where we use the definition of the mass quadrupole used in Owen 2005, and defined in Ushomirsky et al. (2000). Alternatively, we can use h_0 to calculate the fiducial ellipticity, defined as

$$\varepsilon = \frac{h_0}{I_{zz}^{\text{fid}}} \left(\frac{c^4 d}{16\pi^2 G f_{\text{rot}}^2}\right) \approx 2.36 \times 10^{-6} \left(\frac{h_0}{10^{-25}}\right) \left(\frac{d}{1\,\text{kpc}}\right) \left(\frac{100\,\text{Hz}}{f_{\text{rot}}}\right)^2 \left(\frac{10^{38}\,\text{kg m}^2}{I_{zz}^{\text{fid}}}\right). \tag{A4}$$

If emission of gravitational radiation via the $l = m = 2$ mass quadrupole is considered to be the sole energy loss mechanism for a pulsar then by equating the gravitational-wave luminosity (see, e.g., Equation (4) of Aasi et al. 2014)

$$\dot{E}_{\text{gw}} = \frac{8\pi^2 c^3}{5G} f_{\text{rot}}^2 h_0^2 d^2 \approx 6.07 \times 10^{29} \left(\frac{f_{\text{rot}}}{100\,\text{Hz}}\right)^2 \left(\frac{h_0}{10^{-25}}\right)^2 \left(\frac{d}{1\,\text{kpc}}\right)^2 \text{W}, \tag{A5}$$

with the loss of kinetic energy inferred from the the first frequency derivative $\dot{f}_{\text{rot}}$ of the pulsar

$$\dot{E}_{\text{KE}} = 4\pi^2 I_{zz}^{\text{fid}} f_{\text{rot}} |\dot{f}_{\text{rot}}| \approx 3.95 \times 10^{30} \left(\frac{I_{zz}^{\text{fid}}}{10^{38}\,\text{kg m}^2}\right) \left(\frac{f_{\text{rot}}}{100\,\text{Hz}}\right) \left(\frac{|\dot{f}_{\text{rot}}|}{10^{-11}\,\text{Hz s}^{-1}}\right) \text{W}, \tag{A6}$$

one can define the spin-down limit on h_0, where

$$h_0^{\text{sd}} = \frac{1}{d} \left(\frac{5}{2} \frac{G I_{zz}^{\text{fid}}}{c^3} \frac{|\dot{f}_{\text{rot}}|}{f_{\text{rot}}}\right)^{1/2} \approx 2.55 \times 10^{-25} \left(\frac{1\,\text{kpc}}{d}\right) \left(\frac{I_{zz}^{\text{fid}}}{10^{38}\,\text{kg m}^2}\right)^{1/2} \left(\frac{100\,\text{Hz}}{f_{\text{rot}}}\right)^{1/2} \left(\frac{|\dot{f}_{\text{rot}}|}{10^{-11}\,\text{Hz s}^{-1}}\right)^{1/2}. \tag{A7}$$

---

[11] http://tempo.sourceforge.net/

By equating Equations (A1) and (A7), we can rearrange and get spin-down limits on Q_{22} as

$$Q_{22}^{\rm sd} = \left(\frac{75}{4096\pi^5} \frac{I_{zz}^{\rm fid} c^5}{G} \frac{\dot{f}_{\rm rot}}{f_{\rm rot}^5} \right)^{1/2} \approx 4.66 \times 10^{32} \left(\frac{I_{zz}^{\rm fid}}{10^{38}\,{\rm kg\,m^2}} \right)^{1/2} \left(\frac{100\,{\rm Hz}}{f_{\rm rot}} \right)^{5/2} \left(\frac{|\dot{f}_{\rm rot}|}{10^{-11}\,{\rm Hz\,s^{-1}}} \right)^{1/2} {\rm kg\,m^2}, \qquad (A8)$$

and ε as

$$\varepsilon^{\rm sd} = \left(\frac{5}{512\pi^4} \frac{c^5}{I_{zz}^{\rm fid} G} \frac{\dot{f}_{\rm rot}}{f_{\rm rot}^5} \right)^{1/2} \approx 6.03 \times 10^{-6} \left(\frac{10^{38}\,{\rm kg\,m^2}}{I_{zz}^{\rm fid}} \right)^{1/2} \left(\frac{100\,{\rm Hz}}{f_{\rm rot}} \right)^{5/2} \left(\frac{|\dot{f}_{\rm rot}|}{10^{-11}\,{\rm Hz\,s^{-1}}} \right)^{1/2}, \qquad (A9)$$

where it is interesting to note that these are independent of the distance to the pulsar.

For a triaxial source not rotating about a principal axis, and emitting via both the $l = 2$, $m = 1$ and the $l = m = 2$ quadrupole modes, the relations between the waveform amplitudes and phases given in Equations (1) and (2) and the source moment of inertia tensor components and Euler orientation angle θ are described in Section 3.1 of Jones (2015). We will not repeat the relationships here, but note that how to convert between the two definitions is described in detail in the Appendix of Pitkin et al. (2015).

B. PRIORS

In this section we will detail the prior probability distributions used on parameters by the *Bayesian* and 5n-vector analysis methods. The use of these priors for the *Bayesian* search is discussed in Pitkin et al. (2017) and the motivation behind some of the prior limits used are discussed in Jones (2015) and Pitkin et al. (2015). For the 5n-vector pipeline, priors are set on signal initial phase ϕ_0 and polarization parameters, ψ, $\cos\iota$, in the computation of upper limits.

For the gravitational-wave specific orientation parameters for searches purely from the $l = m = 2$ mode, the following priors have been used.[12] The initial rotational phase of the pulsar at a given epoch ϕ_0, the polarization angle ψ, and the cosine of the inclination angle $\cos\iota$ have uniform priors[13] given by

$$\phi_0 \sim \mathcal{U}(0, \pi),$$
$$\psi \sim \mathcal{U}(0, \pi/2),$$
$$\cos\iota \sim \mathcal{U}(-1, 1).$$

For the *Bayesian* search, the prior on the gravitational-wave amplitude h_0 is given by a Fermi-Dirac-type probability distribution (see, e.g., that used in Middleton et al. 2016) described in Pitkin et al. (2017), which has a flat region followed by an exponential decay region, but is non-zero for all positive values. This is parametrized by μ, which gives the value at which the distribution decays to 50% of its maximum value, and σ, which controls the width of the band over which the bulk of the decay happens. The band around μ over which the probability density falls from 97.5% to 2.5% of its peak value is given by $\mu \pm 7.33\mu/2r$, where $r = \mu/\sigma$. In our case we specify that this fall-off happens over a range that is 40% of the value of μ, so that $r = 7.33/(2 \times 0.4) = 9.1625$. The value of μ is set by finding the value that produces a specific bound within which 95% of the probability is constrained (bounded by zero at the lower end) given the previous value of r. The specific bound is that based on the sensitivity for each pulsar (i.e., the 95% upper limits on h_0, see Appendix C) that would have been expected if using data from the sixth LIGO science run, and fourth Virgo science run, scaled up by a factor of 25 to be conservative and make sure that the likelihood is well within the flat part of the prior distribution, while disfavoring arbitrarily large values.[14]

For the searches that include both the $l = 2$, $m = 1, 2$ modes the phase and orientation angle priors have been given by

$$\Phi_{21}^C \sim \mathcal{U}(0, 2\pi),$$
$$\Phi_{22}^C \sim \mathcal{U}(0, 2\pi),$$
$$\psi \sim \mathcal{U}(0, \pi/2),$$
$$\cos\iota \sim \mathcal{U}(-1, 1).$$

---

[12] In the notation used here $\sim$ stands for "has the probability distribution of", and $\mathcal{U}(a, b)$ is a continuous uniform distribution with a constant probability $1/(b - a)$ for $x \in [a, b]$.

[13] The polarization angle ψ, and orientation angle ι, have a joint prior that is uniform over a sphere, with degeneracies when thinking purely in terms of the gravitational-wave waveforms described in Jones (2015), but these can be re-parametrized to independent uniform priors if in terms of $\cos\iota$.

[14] A discussion about a choice between a uniform prior and a uniform in logarithm prior, for the amplitude parameter is given in Appendix B of Isi et al. (2017).

As discussed above, in the *Bayesian* method the priors on the amplitude parameters C_{21} and C_{22} have used Fermi-Dirac probability distributions for which the parameters have been set in the same way as done for h_0. However, in this case the sensitivity estimate used for h_0 is assumed to be valid for C_{21} and C_{22}, while in reality there are factors of a few differences. These differences are allowable given the scaling factor used, and the sensitivity improvements over S6.

In our searches we make use of the pulsar rotational phase parameters (frequency, frequency derivatives, sky location, proper motion, and Keplerian and relativistic binary system orbital parameters if relevant) derived from electromagnetic observation of pulse times-of-arrival. These parameters are obtained by fitting the phase model to the times-of-arrival using software such as TEMPO2 Hobbs et al. (2006) to produce ephemeris files, and these fits include uncertainty estimates. In most cases, and where it is computationally feasible, for any combination of parameters in the ephemeris files that have been re-fit (i.e., a new estimate has been performed using data that matched the requirements of our search, such as being concurrent with the LIGO observing runs) we include a multivariate Gaussian prior in our analysis, for which the diagonal of the covariance matrix is derived from the uncertainties in the ephemeris file and taking them to be one standard deviation values. In the prior covariance matrix we assume no correlations between parameters except in two pairs of cases for pulsars in binary systems; for very low eccentricity systems ($e < 0.001$) with re-fitted uncertainties on both the time and angle of periastron, or with re-fitted values on the period and time derivative of the angle of periastron, the covariance matrix is set such as to make these pairs fully correlated.

As described in Abbott et al. (2010); Aasi et al. (2014); Abbott et al. (2017a), there are some pulsars for which we can place tighter constraints on their orientation. In particular the inclination angle and polarization angle can be assumed to be measured by modelling X-ray observations of their surrounding pulsar wind nebulae (Ng & Romani 2004, 2008). In this analysis, for PSRs J0205+6449, J0534+2200, J0835−4510, J1952+3252, and J2229+6114, in addition to a search using the above priors, we also perform parameter estimation using the restricted priors given in Table 3 of Abbott et al. (2017a), based on values taken from Ng & Romani (2008). In these cases the priors are on the inclination angle ι rather than its cosine. The prior probability distribution on ψ is a unimodal Gaussian, but that on ι is given by the sum of a pair of Gaussian distributions with different means, which is required to account for the fact that rotation direction of the stars are unknown (Jones 2015).

C. SENSITIVITY ESTIMATES

Here we will describe the expected sensitivity of the *Bayesian* analysis in searches for signals purely from the $l = m = 2$ mode, and for coherent searches for signals at both the $l = 2$, $m = 1, 2$ modes. We define the expected sensitivity based on the observation time ($T_{\rm obs}$) weighted noise power spectral density $S_n(f)$ as a function of frequency f, such that for a single detector

$$\langle h(f) \rangle = D\sqrt{\frac{S_n(f)}{T_{\rm obs}}}, \tag{C10}$$

where in our case $\langle h(f) \rangle$ is the expected 95% credible upper limit on amplitude and D is an empirically derived scaling factor (similar to the sensitivity depth defined in Behnke et al. 2015). When combining data from multiple detectors and observing runs, for which the power spectral densities will be different, we take the harmonic mean of the time weighted power spectral densities. For example, for a set of different noise power spectral densities $S_{n_i}(f)$ associated with observation times $T_{{\rm obs}_i}$ we would have

$$\langle h(f) \rangle = D\left(\sum_{i=1}^{N}\left[\frac{S_{n_i}(f)}{T_{{\rm obs}_i}}\right]^{-1}\right)^{-1/2}. \tag{C11}$$

For a search for emission from the $l = m = 2$ mode, where the limit is on the gravitational-wave amplitude h_0 (see Equation (A1)) it was shown in Dupuis & Woan (2005) that $D \approx 10.8 \pm 0.2$, based on the simulations containing purely Gaussian noise with variance drawn from a known power spectral density, marginalised over orientations and averaged over the sky. If we instead take the median rather than the mean over a similar set of simulations, to suppress any outlier values, we find $D \approx 10.4$ (see left-most panel of Figure 5), which is used here in producing the sensitivity curve in Figure 2.

To estimate the sensitivity to the C_{21} and C_{22} amplitude parameters for a $l = 2$, $m = 1, 2$ mode search we have performed similar simulations to those described above. A search including both modes is not completely independent
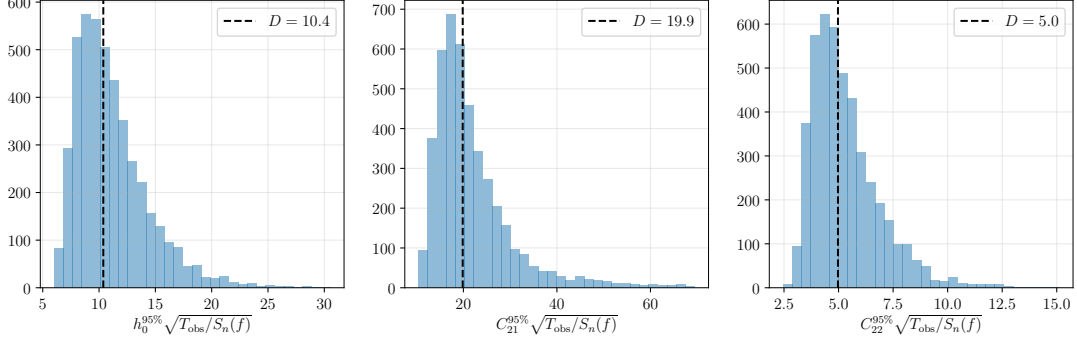
Figure 5. Distributions of 95% credible upper limits on h_0 (left), C_{21} (middle) and C_{22} (right) scaled by the observation times and noise power spectral density for a set of simulations consisting of Gaussian noise. To average over effects of different antenna patterns in performing parameter estimation each simulation assumes a random source sky location for a uniform distribution over the sky.
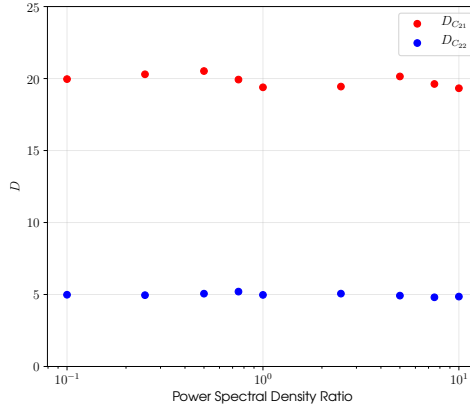

Figure 6. The D scale factor for the C_{21} and C_{22} upper limits as a function of the power spectral density ratio between the data at equivalents of the rotation frequency and twice the rotation frequency.

for each mode as there are common orientation parameters. So, we also wanted to investigate whether the sensitivity at either amplitude is affected by the noise level at the other amplitude. We generated simulations consisting of independent Gaussian noise in two data streams; one equivalent to the data at the rotation frequency and another equivalent to the data at twice the rotation frequency. For the data stream at twice the rotation frequency the noise was always drawn from a Gaussian distribution with the same variance defined by a power spectral density of $10^{-48}\,\mathrm{Hz}^{-1/2}$. For the data stream at the rotation frequency we created multiple sets of 500 instantiations where the noise was drawn from a Gaussian distribution with a variance defined by a power spectral density of $10^{-48}x\,\mathrm{Hz}^{-1/2}$, where for each set of 500 x was a different factor between 0.1 and 10. The D scale factor from Equation (C10) for both the C_{21} and C_{22} amplitude upper limit for each set of 500 simulations and as a function of x is shown in Figure 6. It can be seen that there is no obvious correlation between the power spectral density ratio x and the value of D, which suggests that the upper limits on the two amplitudes are actually largely independent.

We see from Figures 5 and 6 that the value of D used to estimate the sensitivity for C_{21} is 19.9, and the value of D used to estimate the sensitivity for C_{22} is 5.0. These values have been used when producing the sensitivity curves in Figure 1.

D. MIXED BAYESIAN-FREQUENTIST UPPER LIMIT COMPUTATION FOR THE $5N$-VECTOR METHOD

Given a measured value S^* of a detection statistic $\mathcal{S}$, the frequentist upper limit at a given confidence level α is defined as that value of signal amplitude h_{ul} such that a signal with amplitude $h_0 > h_{\mathrm{ul}}$ produces a value of the
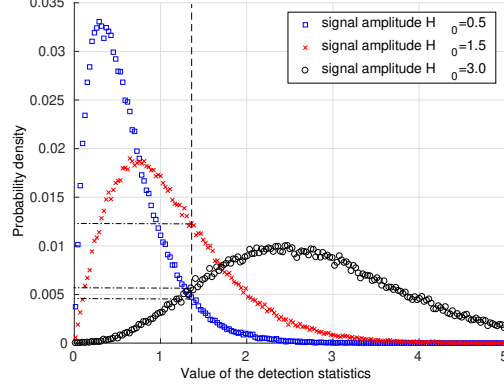
Figure 7. Probability distributions of the detection statistic $\mathcal{S}$ after having injected into Gaussian noise with $\sigma=1$ signals with three different amplitudes. Given the measured value of the detection statistic $\mathcal{S}^*$ (shown by the vertical dashed line), the corresponding values of probability density for the various signal amplitudes are determined (shown by the horizontal dot-dashed lines).

detection statistic bigger than S^* in a fraction α of a large number of repeated experiments: $P(S > S^*|h_0 > h_{\rm ul}) = \alpha$. Typically, the upper limit is computed using Neymans rule for the construction of confidence intervals (Neyman 1937). This classical frequentist upper limit has the following well-known and unpleasant feature: if the value of the detection statistic S^* falls in the first 1-α quantile of its noise-only distribution the resulting upper limit is exactly zero. This behavior, although legitimate in the frequentist framework, poses a problem for instance when upper limits obtained in the analysis of datasets with different sensitivity are compared. It may happen that, due to a noise fluctuation, the upper limit set for the more noisy data is lower than that computed for the less noisy one. This kind of problem may happen also for Bayesian upper limits but it is exacerbated in the classical frequentist case.

The unwanted features of the classical Neymans construction have been overcome in the Feldman-Cousins unified approach where, using the freedom inherent in Neymans construction, a method to obtain a unified set of classical confidence intervals for computing both upper limits and two-sided confidence intervals has been obtained (Feldman & Cousins 1998). The Feldman-Cousins approach sometimes is difficult to implement, and, similarly to the Neyman's approach, does not allow accounting for non-uniform prior distributions for nuisance parameters.

We have developed an alternative method for setting upper limits on signal amplitude which keeps the advantages of the frequentist approach, like the ease of implementation and computational speed while avoiding its problems. The basic idea is that of computing the posterior distribution of the signal amplitude conditioned to the measured value of the detection statistic. The main steps of the procedure can be summarized as follows.

We consider a set of possible signal amplitudes H_0. For each amplitude we generate several signals with polarization parameters distributed according to given prior distributions and for each signal we compute the corresponding value of the detection statistic. Hence the probability distribution of the detection statistic, for the different signal amplitudes, can be built, see Figure 7. For each distribution we determine the value corresponding to the measured detection statistic $p(S^*|H_0)$. By multiplying each value by the prior probability density of the signal amplitude, $p(H_0)$ and normalizing we obtain the posterior probability distribution for the signal amplitude: $p(H_0|S^*) \propto p(S^*|H_0)p(H_0)$, see Figure 8.

We then calculate the cumulative probability distribution and obtain the amplitude value corresponding to a given probability, e.g. 0.95, see Figure 9. This is the 95% credible upper limit.

E. AMPLITUDE CONVERSION FACTORS FOR THE 5N-VECTOR METHOD

The 5n-vector method uses a non-standard formalism to describe the gravitational-wave signal, based on the concept of polarization ellipse (Astone et al. 2010; Abadie et al. 2011; Aasi et al. 2014). In this formalism the signal strain is given by the real part of

$$h(t) = H_0(H_+\mathbf{e}^+ + H_\times\mathbf{e}^\times)e^{\imath(\omega_0(t)t+\Phi_0)} \tag{E12}$$
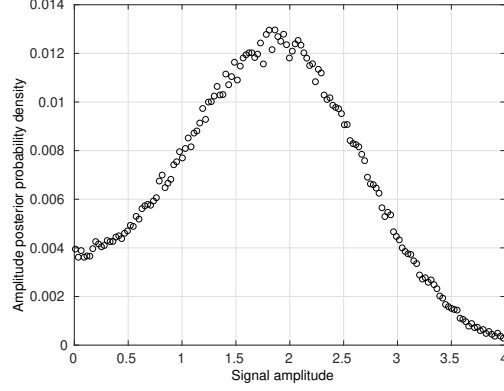
Figure 8. Posterior probability distribution of the signal amplitude for the given measured value S* of the detection statistic.
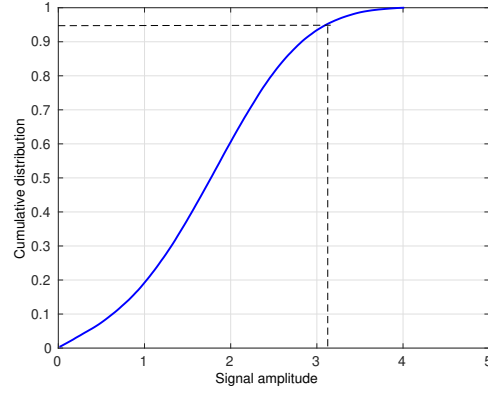

Figure 9. Cumulative posterior probability distribution of the signal amplitude. The amplitude value corresponding to 95% of the cumulative is the wanted credible upper limit.

where $\omega_0(t)$ is the signal angular frequency, $\mathbf{e}^{+/\times}$ are the two basis polarization tensors, Φ_0 the signal phase at the time $t = 0$, and the two complex amplitudes H_+, $H_\times$ are given by

$$H_+ = \frac{\cos 2\psi - \imath\eta \sin 2\psi}{\sqrt{1 + \eta^2}}, \ H_\times = \frac{\sin 2\psi + \imath\eta \cos 2\psi}{\sqrt{1 + \eta^2}}, \tag{E13}$$

in which $\eta \in [-1, 1]$ is the ratio of the polarization ellipse semi-minor to semi-major axis and the polarization angle ψ defines, as usual, the direction of the major axis with respect to the celestial parallel of the source (measured counterclockwise). The signal described by Equation (E12) is general, i.e., does not assume any specific emission mechanism by a spinning neutron star. Assuming a triaxial star spinning about a principal axis of inertia, the overall amplitude H_0 is related to the standard h_0 by

$$h_0 = \frac{2H_0}{\sqrt{1 + 6\cos^2 \iota + \cos^4 \iota}}. \tag{E14}$$

For the emission at the star's rotational frequency of the $l = 2$, $m = 1$ harmonic mode (see Equation (1)), the relation between H_0 and the amplitude C_{21} is given by

$$C_{21} = \frac{2H_0}{\sqrt{1 - \cos^4 \iota}} \tag{E15}$$

As discussed in, e.g., Aasi et al. (2014), upper limits are computed on H_0 and then converted to h_0 or C_{21} using Equations (E14) and (E15) where the functions of ι are replaced by their mean value: $h_0^{95\%} \simeq 1.37 H_0^{95\%}$, and $C_{21}^{95\%} \simeq 1.31 H_0^{95\%}$.

REFERENCES

Aasi, J., Abadie, J., Abbott, B. P., et al. 2014, ApJ, 785, 119, doi: 10.1088/0004-637X/785/2/119

Aasi, J., Abbott, B. P., Abbott, R., et al. 2015a, PhRvD, 91, 022004, doi: https://doi.org/10.1103/PhysRevD.91.022004

—. 2015b, CQGra, 32, 074001, doi: 10.1088/0264-9381/32/7/074001

Abadie, J., Abbott, B. P., Abbott, R., et al. 2011, ApJ, 737, 93, doi: 10.1088/0004-637X/737/2/93

Abbott, B., Abbott, R., Adhikari, R., et al. 2004, PhRvD, 69, 082004, doi: 10.1103/PhysRevD.69.082004

—. 2005, PhRvL, 94, 181103, doi: 10.1103/PhysRevLett.94.181103

—. 2007, PhRvD, 76, 042001, doi: 10.1103/PhysRevD.76.042001

—. 2008, ApJL, 683, L45, doi: 10.1086/591526

Abbott, B. P., Abbott, R., Adhikari, R., et al. 2009, RPPh, 72, 076901, doi: 10.1088/0034-4885/72/7/076901

Abbott, B. P., Abbott, R., Acernese, F., et al. 2010, ApJ, 713, 671, doi: 10.1088/0004-637X/713/1/671

Abbott, B. P., Abbott, R., Abbott, T. D., et al. 2016, PhRvL, 116, 131103, doi: 10.1103/PhysRevLett.116.131103

—. 2017a, ApJ, 839, 12, doi: 10.3847/1538-4357/aa677f

—. 2017b, PhRvD, 96, 122006, doi: 10.1103/PhysRevD.96.122006

—. 2017c, PhRvL, 119, 161101, doi: 10.1103/PhysRevLett.119.161101

—. 2017d, PhRvL, 119, 141101, doi: 10.1103/PhysRevLett.119.141101

—. 2018a, PhRvL, 120, 031104, doi: 10.1103/PhysRevLett.120.031104

—. 2018b, PhRvL, 121, 161101, doi: 10.1103/PhysRevLett.121.161101

Accadia, T., Acernese, F., Alshourbagy, M., et al. 2012, JInst, 7, 3012, doi: 10.1088/1748-0221/7/03/P03012

Acernese, F., Agathos, M., Agatsuma, K., et al. 2015, CQGra, 32, 024001, doi: 10.1088/0264-9381/32/2/024001

Antoniadis, J., Freire, P. C. C., Wex, N., et al. 2013, Sci, 340, 448, doi: 10.1126/science.1233232

Arzoumanian, Z., Brazier, A., Burke-Spolaor, S., et al. 2018, ApJS, 235, 37, doi: 10.3847/1538-4365/aab5b0

Astone, P., Colla, A., D'Antonio, S., Frasca, S., & Palomba, C. 2012, JPhCS, 363, 012038, doi: 10.1088/1742-6596/363/1/012038

Astone, P., D'Antonio, S., Frasca, S., & Palomba, C. 2010, CQGra, 27, 194016, doi: 10.1088/0264-9381/27/19/194016

Bassa, C. G., Antoniadis, J., Camilo, F., et al. 2016, MNRAS, 455, 3806, doi: 10.1093/mnras/stv2607

Behnke, B., Papa, M. A., & Prix, R. 2015, PhRvD, 91, 064007, doi: 10.1103/PhysRevD.91.064007

Bejger, M. 2013, A&A, 552, A59, doi: 10.1051/0004-6361/201220876

Bejger, M., & Królak, A. 2014, CQGra, 31, 105011, doi: 10.1088/0264-9381/31/10/105011

Bogdanov, S., Ho, W. C. G., Enoto, T., et al. 2019, arXiv:1902.00144

Bonazzola, S., & Gourgoulhon, E. 1996, A&A, 312, 675

Boyles, J., Lynch, R. S., Ransom, S. M., et al. 2013, ApJ, 763, 80, doi: 10.1088/0004-637X/763/2/80

Braga, V. F., Dall'Ora, M., Bono, G., et al. 2015, ApJ, 799, 165, doi: 10.1088/0004-637X/799/2/165

Cahillane, C., Hulko, M., Kissel, J. S., et al. 2018, LIGO G1800319 https://dcc.ligo.org/LIGO-G1800319/public

Cahillane, C., Betzwieser, J., Brown, D. A., et al. 2017, PhRvD, 96, 102001, doi: 10.1103/PhysRevD.96.102001

Caplan, M. E., Schneider, A. S., & Horowitz, C. J. 2018, PhRvL, 121, 132701, doi: 10.1103/PhysRevLett.121.132701

Cordes, J. M., & Lazio, T. J. W. 2002, arXiv:astro-ph/0207156

Cutler, C. 2002, PhRvD, 66, 084025, doi: 10.1103/PhysRevD.66.084025

Damour, T., & Taylor, J. H. 1991, ApJ, 366, 501, doi: 10.1086/169585

Davis, D., Massinger, T. J., Lundgren, A. P., et al. 2018, ArXiv e-prints. https://arxiv.org/abs/1809.05348

Deller, A. T., Bailes, M., & Tingay, S. J. 2009, Sci, 323, 1327, doi: 10.1126/science.1167969

Deller, A. T., Boyles, J., Lorimer, D. R., et al. 2013, ApJ, 770, 145, doi: 10.1088/0004-637X/770/2/145

Desvignes, G., Caballero, R. N., Lentati, L., et al. 2016, MNRAS, 458, 3341, doi: 10.1093/mnras/stw483

Dodson, R., Legge, D., Reynolds, J. E., & McCulloch, P. M. 2003, ApJ, 596, 1137, doi: 10.1086/378089

30

Driggers, J. C., Vitale, S., Lundgren, A. P., et al. 2018, arXiv:1806.00532

Dupuis, R. J., & Woan, G. 2005, PhRvD, 72, 102002, doi: 10.1103/PhysRevD.72.102002

Durant, M., Kargaltsev, O., Pavlov, G. G., Kropotina, J., & Levenfish, K. 2013, ApJ, 763, 72, doi: 10.1088/0004-637X/763/2/72

Espinoza, C. M., Lyne, A. G., Stappers, B. W., & Kramer, M. 2011, MNRAS, 414, 1679, doi: 10.1111/j.1365-2966.2011.18503.x

Espinoza, C. M., Guillemot, L., Çelik, Ö., et al. 2013, MNRAS, 430, 571, doi: 10.1093/mnras/sts657

Fattoyev, F. J., Horowitz, C. J., & Lu, H. 2018, arXiv:1804.04952

Feldman, G. J., & Cousins, R. D. 1998, PhRvD, 57, 3873, doi: 10.1103/PhysRevD.57.3873

Ferdman, R. D., Stairs, I. H., Kramer, M., et al. 2014, MNRAS, 443, 2183, doi: 10.1093/mnras/stu1223

Fonseca, E., Stairs, I. H., & Thorsett, S. E. 2014, ApJ, 787, 82, doi: 10.1088/0004-637X/787/1/82

Freire, P. C. C., Abdo, A. A., Ajello, M., et al. 2011, Science, 334, 1107, doi: 10.1126/science.1207141

Freire, P. C. C., Wex, N., Esposito-Farèse, G., et al. 2012, MNRAS, 423, 3328, doi: 10.1111/j.1365-2966.2012.21253.x

Gotthelf, E. V., Halpern, J. P., Terrier, R., & Mattana, F. 2011, ApJ, 729, L16, doi: 10.1088/2041-8205/729/2/L16

Gratton, R. G., Bragaglia, A., Carretta, E., et al. 2003, A&A, 408, 529, doi: 10.1051/0004-6361:20031003

Halpern, J. P., Bogdanov, S., & Gotthelf, E. V. 2013, ApJ, 778, 120, doi: 10.1088/0004-637X/778/2/120

Halpern, J. P., Gotthelf, E. V., Leighly, K. M., & Helfand, D. J. 2001, ApJ, 547, 323, doi: 10.1086/318361

Harris, W. E. 1996, VizieR Online Data Catalog, 7195

Hobbs, G. B., Edwards, R. T., & Manchester, R. N. 2006, MNRAS, 369, 655, doi: 10.1111/j.1365-2966.2006.10302.x

Horowitz, C. J. 2010, PhRvD, 81, 103001, doi: 10.1103/PhysRevD.81.103001

Hunter, J. D. 2007, CSE, 9, 90, doi: 10.1109/MCSE.2007.55

Isi, M., Pitkin, M., & Weinstein, A. J. 2017, PhRvD, 96, 042001, doi: 10.1103/PhysRevD.96.042001

Jaranowski, P., & Królak, A. 2010, CQGra, 27, 194015, doi: 10.1088/0264-9381/27/19/194015

Jaranowski, P., Królak, A., & Schutz, B. F. 1998, PhRvD, 58, 063001, doi: 10.1103/PhysRevD.58.063001

Johnson, T. J., Guillemot, L., Kerr, M., et al. 2013, ApJ, 778, 106, doi: 10.1088/0004-637X/778/2/106

Johnson-McDaniel, N. K. 2013, PhRvD, 88, 044016, doi: 10.1103/PhysRevD.88.044016

Johnson-McDaniel, N. K., & Owen, B. J. 2013, PhRvD, 88, 044004, doi: 10.1103/PhysRevD.88.044004

Jones, D. I. 2010, MNRAS, 402, 2503, doi: 10.1111/j.1365-2966.2009.16059.x

—. 2012, MNRAS, 420, 2325, doi: 10.1111/j.1365-2966.2011.20238.x

—. 2015, MNRAS, 453, 53, doi: 10.1093/mnras/stv1584

Jones, D. I., & Andersson, N. 2002, MNRAS, 331, 203, doi: 10.1046/j.1365-8711.2002.05180.x

Kothes, R. 2013, A&A, 560, A18, doi: 10.1051/0004-6361/201219839

LIGO Scientific Collaboration. 2018, LIGO Algorithm Library, Caltech Library, doi: 10.7935/GT1W-FZ16

Manchester, R. N., Hobbs, G. B., Teoh, A., & Hobbs, M. 2005, AJ, 129, 1993, doi: 10.1086/428488

Marelli, M., Harding, A., Pizzocaro, D., et al. 2014, ApJ, 795, 168, doi: 10.1088/0004-637X/795/2/168

Mastrano, A., & Melatos, A. 2012, MNRAS, 421, 760, doi: 10.1111/j.1365-2966.2011.20350.x

McNamara, B. J., Harrison, T. E., & Baumgardt, H. 2004, ApJ, 602, 264, doi: 10.1086/380905

Melatos, A., & Phinney, E. S. 2001, PASA, 18, 421, doi: 10.1071/AS01056

Middleton, H., Del Pozzo, W., Farr, W. M., Sesana, A., & Vecchio, A. 2016, MNRAS, 455, L72, doi: 10.1093/mnrasl/slv150

Mingarelli, C. M. F., Anderson, L., Bedell, M., & Spergel, D. N. 2018, arXiv:1812.06262

Neyman, J. 1937, Philosophical Transactions of the Royal Society of London. Series A, Mathematical and Physical Sciences, 236, 333, doi: 10.1098/rsta.1937.0005

Ng, C., Bailes, M., Bates, S. D., et al. 2014, MNRAS, 439, 1865, doi: 10.1093/mnras/stu067

Ng, C.-Y., & Romani, R. W. 2004, ApJ, 601, 479, doi: 10.1086/380486

—. 2008, ApJ, 673, 411, doi: 10.1086/523935

Ortolani, S., Barbuy, B., Bica, E., Zoccali, M., & Renzini, A. 2007, A&A, 470, 1043, doi: 10.1051/0004-6361:20066628

Ostriker, J. P., & Gunn, J. E. 1969, ApJ, 157, 1395, doi: 10.1086/150160

Owen, B. J. 2005, Physical Review Letters, 95, 211101, doi: 10.1103/PhysRevLett.95.211101

Palfreyman, J. 2016, ATel, 9847

Palfreyman, J., Dickey, J. M., Hotan, A., Ellingsen, S., & van Straten, W. 2018, Natur, 556, 219, doi: 10.1038/s41586-018-0001-x

Palomba, C. 2000, A&A, 354, 163

Payne, D. J. B., & Melatos, A. 2004, MNRAS, 351, 569, doi: 10.1111/j.1365-2966.2004.07798.x

Pitkin, M., Gill, C., Jones, D. I., Woan, G., & Davies, G. S. 2015, MNRAS, 453, 4399, doi: 10.1093/mnras/stv1931

Pitkin, M., Isi, M., Veitch, J., & Woan, G. 2017, arXiv:1705.08978

Pitkin, M., Messenger, C., & Fan, X. 2018, PhRvD, 98, 063001, doi: 10.1103/PhysRevD.98.063001

Reardon, D. J., Hobbs, G., Coles, W., et al. 2016, MNRAS, 455, 1751, doi: 10.1093/mnras/stv2395

Rees, R. F., & Cudworth, K. M. 1991, AJ, 102, 152, doi: 10.1086/115863

Romani, R. W., & Shaw, M. S. 2011, ApJL, 743, L26, doi: 10.1088/2041-8205/743/2/L26

Shklovskii, I. S. 1970, Soviet Ast., 13, 562

Spiewak, R., Bailes, M., Barr, E. D., et al. 2018, MNRAS, 475, 469, doi: 10.1093/mnras/stx3157

Ushomirsky, G., Cutler, C., & Bildsten, L. 2000, MNRAS, 319, 902, doi: 10.1046/j.1365-8711.2000.03938.x

Valenti, E., Ferraro, F. R., & Origlia, L. 2007, AJ, 133, 1287, doi: 10.1086/511271

—. 2010, MNRAS, 402, 1729, doi: 10.1111/j.1365-2966.2009.15991.x

Vallisneri, M., Kanner, J., Williams, R., Weinstein, A., & Stephens, B. 2015, JPhCS, 610, 012021, doi: 10.1088/1742-6596/610/1/012021

Verbiest, J. P. W., & Lorimer, D. R. 2014, MNRAS, 444, 1859, doi: 10.1093/mnras/stu1560

Verbiest, J. P. W., Weisberg, J. M., Chael, A. A., Lee, K. J., & Lorimer, D. R. 2012, ApJ, 755, 39, doi: 10.1088/0004-637X/755/1/39

Vigeland, S. J., Deller, A. T., Kaplan, D. L., et al. 2018, ApJ, 855, 122, doi: 10.3847/1538-4357/aaaa73

Wang, W. 2011, Research in Astronomy and Astrophysics, 11, 824, doi: 10.1088/1674-4527/11/7/007

Woan, G., Pitkin, M. D., Haskell, B., Jones, D. I., & Lasky, P. D. 2018, ApJL, 863, L40, doi: 10.3847/2041-8213/aad86a

Worley, A., Krastev, P. G., & Li, B.-A. 2008, ApJ, 685, 390, doi: 10.1086/589823

Yao, J. M., Manchester, R. N., & Wang, N. 2017, ApJ, 835, 29, doi: 10.3847/1538-4357/835/1/29

Zimmermann, M. 1980, PhRvD, 21, 891, doi: 10.1103/PhysRevD.21.891

Zimmermann, M., & Szedenits, Jr., E. 1979, PhRvD, 20, 351, doi: 10.1103/PhysRevD.20.351